

1 **How do variably striking faults reactivate during rifting? Insights from southern**  
2 **Malawi**

3  
4 Jack N. Williams<sup>1\*</sup>, Åke Fagereng<sup>1</sup>, Luke N. J. Wedmore<sup>2</sup>, Juliet Biggs<sup>2</sup>, Felix Mphepo<sup>3</sup>,  
5 Zuze Dulanya<sup>4</sup>, Hassan Mdala<sup>3</sup>, Tom Blenkinsop<sup>1</sup>

6  
7 <sup>1</sup>*School of Earth and Ocean Sciences, Cardiff University, Cardiff, UK*

8 <sup>2</sup>*School of Earth Sciences, University of Bristol, Bristol, UK*

9 <sup>3</sup>*Geological Survey Department, Mzuzu Regional Office, Mzuzu, Malawi*

10 <sup>4</sup>*Geography and Earth Sciences Department, University of Malawi, Zomba, Malawi*

11  
12 \*Corresponding author: Jack Williams ([williamsj132@cardiff.ac.uk](mailto:williamsj132@cardiff.ac.uk))

13  
14 *This manuscript is a non-reviewed preprint deposited on the EarthArxiv platform that has*  
15 *been submitted to Geochemistry, Geophysics, Geosystems.*

16  
17 **Key points**

- 18
- 19 • Stress states at the southern end of the Malawi Rift are tested by assessing fault  
20 reactivation potential.
  - 21 • Variably oriented rift faults reactivate by all striking slightly obliquely to an E-W  
22 trending minimum principal compressive stress.
  - 23 • Faults may locally accommodate pure normal dip-slip due to the presence of a deep  
24 seated crustal weakness.

## 25 **Abstract**

26 Active normal faults at the southern end of the Malawi Rift follow an arcuate bend in the  
27 high grade metamorphic foliation, with strikes ranging from NW to NNE. However, previous  
28 estimates of the stress state that allows such a wide range of normal fault strikes to reactivate  
29 are enigmatic, as both a NW-SE and NE-SW trending minimum compressive stress ( $\sigma_3$ ) have  
30 been proposed. Furthermore, we present field observations of a consistently N-S striking sub-  
31 vertical joint set in southern Malawi, which suggests an E-W trending  $\sigma_3$ . We address this  
32 problem by calculating the stress ratio ( $\sigma_3/\sigma_1$ , where  $\sigma_1$  is the maximum compressive stress)  
33 and effective coefficient of friction ( $\mu_s'$ ) required to reactivate the rift's variably striking  
34 faults in stress states based on earthquake focal mechanisms (Stress State 1:  $\sigma_3=06/242$ ) and  
35 joint sets (Stress State 2:  $\sigma_3=00/082$ ). Given the consistency of joint orientations, we infer a  
36 uniform stress state and reject an alternative hypothesis that  $\sigma_3$  rotates along the rift. In Stress  
37 State 1, NW-striking faults are well oriented. However, misoriented NNE-striking faults  
38 require  $\mu_s' < 0.7$  to reactivate, which is inconsistent with the lack of frictionally weak  
39 phyllosilicates detected in compositional analysis of these faults. In Stress State 2, all faults  
40 are well oriented and can reactivate at  $\mu_s' > 0.6$ . This is also comparable to a previously  
41 reported geodetically-derived extension direction. Stress State 2 is therefore favoured,  
42 indicating that the southern Malawi Rift consists of a series of slightly-oblique basins, and  
43 not alternating orthogonal and highly-oblique sections as predicted by typical models of  
44 oblique rifting.

45

## 46 **Plain Language Summary**

47 Stretching of the upper brittle part of the Earth's crust should be accommodated by cracks  
48 (faults) oriented at  $90^\circ$  to the stretching direction. However, this idealized scenario is rarely  
49 observed because the crust is often mechanically heterogenous, or because the stretching  
50 direction rotates over geological time. Thus, faults are often non-orthogonal (i.e. oblique) to  
51 the stretching direction. Here, we use a mechanical analysis to test the obliquity of faults in  
52 southern Malawi at the southern juvenile end of the East African Rift system where the crust  
53 is actively extending at  $\sim 2$  mm/yr. This section is of interest as fault orientation varies along  
54 the rift, and a range of stretching directions have been proposed previously. Our mechanical  
55 analysis indicates that extension is most likely accommodated in southern Malawi by faults  
56 that are all slightly oblique to an E-W stretching direction. This is in contrast to previous  
57 models of oblique rifting, which suggest that stretching is accommodated by some faults at  
58  $90^\circ$  to the stretching direction, whilst others are at a very low ( $< 40^\circ$ ) angle to stretching.

59

## 60 **Key words**

61 Continental rift, East African Rift, Fault reactivation, Tectonic stress, Normal faults, Stress  
62 inversions

63

## 64 **1. Introduction**

65 The axis of a continental rift is expected to be orthogonal to the minimum principal  
66 compressive stress ( $\sigma_3$ ). This is, however, rarely the case [Brune *et al.*, 2018] due to factors  
67 such as temporal stress rotations since the inception of the rifting [Bellahsen *et al.*, 2006;  
68 Henstra *et al.*, 2015], or pre-existing crustal fabrics that present cohesionless [Etheridge,  
69 1986; Morley *et al.*, 2004] or frictionally-weak planes [Massironi *et al.*, 2011]. These spatial

70 and temporal heterogeneities allow a much greater range of fault orientations, which strike  
71 oblique to  $\sigma_3$  and do not contain the intermediate principal compressive stress ( $\sigma_2$ ).

72  
73 Often, obliquely oriented rifts will contain faults with a wide range of strikes, whereby some  
74 faults strike orthogonal to  $\sigma_3$  and are linked oblique-slip or strike-slip transfer zones where  
75 faults striking highly obliquely to  $\sigma_3$  [Acocella *et al.*, 1999; Bellahsen & Daniel, 2005;  
76 McClay & White, 1995; Withjack & Jamison, 1986], as has been proposed in the East African  
77 Rift [Corti, 2012; Delvaux, 2001], Rio Grande Rift [Aldrich, 1986], Rhine Graben  
78 [Chorowicz & Deffontaines, 1993; Lopes Cardozo & Behrmann, 2006], and the Gulf of Aden  
79 [Bellahsen *et al.*, 2006]. The stress directions in these rifts are typically inferred from  
80 measurements of incremental fault strain (i.e. fault slickensides, earthquake focal  
81 mechanisms). This is justified by the Wallace-Bott criterion, which predicts that fault slip is  
82 parallel to the direction of maximum resolved shear stress on a fault plane [Bott, 1959;  
83 Wallace, 1951]. However, this criterion can break down [Pollard *et al.*, 1993; Twiss &  
84 Unruh, 1998], including cases whereby rift faults that strike oblique to the regional  $\sigma_3$  trend  
85 accommodate pure normal dip-slip [Corti *et al.*, 2013; Morley, 2010; Petit *et al.*, 1996;  
86 Philippon *et al.*, 2015]. Deriving stress states in rifts from fault-hosted slickensides is further  
87 complicated because dip-slip faults can host oblique-slip and even strike-slip components due  
88 to convergent patterns of co-seismic slip [Hampel *et al.*, 2013; Philippon *et al.*, 2015].

89  
90 In this study, we address the problem of resolving stress states in rifts with variably striking  
91 faults by assuming *a priori* different stress states, and then interpreting their applicability in  
92 terms of fault reactivation potential. We use the southern end of the Malawi Rift (Figure 1) as  
93 a case example, as geological maps [Bloomfield & Garson, 1965; Habgood *et al.*, 1973;  
94 Walshaw, 1965], fault scarps [Hodge *et al.*, 2019; Wedmore *et al.*, in prep.], and earthquake  
95 focal mechanisms [Delvaux & Barth, 2010] demonstrate that active faults switch from  
96 dominantly NW-SE striking in the Makanjira Graben to NNE-SSW in the Zomba Graben and  
97 then back to NW-SE in the Lower Shire Graben as the rift follows an arcuate bend in the high  
98 grade metamorphic foliation (Figure 2). Furthermore, there is an inconsistency in the regional  
99  $\sigma_3$  trend when inferred from fault slickensides [Chorowicz & Sorlien, 1992], fault geometry  
100 [Mortimer *et al.*, 2007], earthquake focal mechanisms [Delvaux & Barth, 2010], and geodetic  
101 models [Stamps *et al.*, 2018]. Here, three possible stress states are considered:

- 102
- 103 • Stress State 1: A uniform stress state where  $\sigma_3$  trends SW (06/242, Figure 2d), as  
104 proposed by an earthquake focal mechanism stress inversion for the Malawi Rift  
105 [Delvaux & Barth, 2010]. In this way, the angle ( $\alpha$ ) between fault strike and  $\sigma_3$  is  
106  $\sim 90^\circ$  for NW-striking faults, whilst for NNE-striking faults  $\alpha$  is  $\sim 40^\circ$ , and thus they  
107 would act as oblique transfer zones.
  - 108 • Stress State 2: A uniform stress state with an  $\sim$ E-W trending  $\sigma_3$  (00/082, Figure 2e),  
109 which is consistent with the extension direction inferred from geodetic models  
110 [Stamps *et al.*, 2018] and regional joint orientations (Figure 2c). Thus, both faults sets  
111 form slightly oblique grabens  $\sigma_3$  ( $\alpha > 60^\circ$ ).
  - 112 • Stress State 3: The stress state is heterogenous in southern Malawi, with Proterozoic  
113 fabrics actively rotating  $\sigma_3$  along the rift so that  $\alpha$  is consistently  $90^\circ$  (Figure 2f;  
114 Morley, [2010]).

115  
116 We first compare these stress states to a new rift-wide stress inversion performed using an  
117 updated compilation of earthquake focal mechanisms and fault slickenside orientations. Then  
118 the reactivation potential of three differently oriented faults in these stress states is

119 determined in terms of their stress ratio, slip tendency, and effective coefficient of friction.  
120 By comparing these results to the frictional properties of the faults inferred from new field  
121 observations and compositional analysis, and deformation experiments performed by  
122 *Hellebrekers et al.*, [in review], we can determine which stress state is most applicable in  
123 southern Malawi. In doing so, new insights are gained into the applicability of using  
124 incremental fault strain measurements in stress inversions, and on the controls on fault  
125 geometry in an incipient rift.  
126

## 127 **2. Geological setting of the southern Malawi Rift**

128 The Malawi Rift is a 900 km long amagmatic section of the East African Rift System's  
129 (EARS) Western Branch, and runs from the Rungwe Province in the north to the Urema  
130 Graben in the south (Figure 1; *Ebinger et al.*, [1987]). It is typically further divided along its  
131 axis into a series of 100-150 km long grabens and half grabens with alternating polarities  
132 [*Ebinger*, 1989; *Ebinger et al.*, 1987; *Flannery & Rosendahl*, 1990; *Laõ-Dávila et al.*, 2015].  
133 The focus of this study are the three southernmost grabens: the Lower Shire, Zomba, and  
134 Makanjira Grabens (Figure 2a).  
135

136 Basement rock within these grabens constitute part of the Southern Irumide Belt (Figure 1), a  
137 structurally complex Mesoproterozoic orogenic belt that underwent amphibolite-granulite  
138 facies metamorphism during the Pan African orogeny (c. 800-450 Ma.; *Kröner et al.*, [2001];  
139 *Johnson et al.*, [2006]; *Fritz et al.*, [2013]). Whether this belt experienced earlier Irumide age  
140 deformation (c. 1020-950 Ma) is unclear [*Andreoli*, 1984; *Fritz et al.*, 2013; *Johnson et al.*,  
141 2006; *Kröner et al.*, 2001] and the Lower Shire graben may strictly be part of the  
142 Neoproterozoic Zambesi Belt [*Chorowicz & Sorlien*, 1992; *Hargrove et al.*, 2003; *Laõ-*  
143 *Dávila et al.*, 2015]. The Lower Shire Graben also underwent NW-SE Karoo extension  
144 (*Habgood*, 1963; *Castaing*, 1991), whereas this extension was comparatively minor further  
145 north in the Zomba Graben [*Bloomfield*, 1965]. This was followed by a major period of  
146 Upper Jurassic-Lower Cretaceous magmatism throughout southern Malawi, which formed  
147 the Chilwa Alkaline Province [*Bloomfield*, 1965; *Castaing*, 1991; *Dulanya*, 2017; *Habgood*,  
148 1963].  
149

150 EARS extension initiated at the northern end of the Malawi Rift c. 8.6 Ma [*Ebinger et al.*,  
151 1993], although a c. 25 Ma has also been proposed [*Mortimer et al.*, 2016; *Roberts et al.*,  
152 2012]. Given the gradual southward propagation of the EARS [*Ebinger et al.*, 1987], the  
153 southern grabens analyzed here are likely younger (<5 Ma) than those further north; however,  
154 there is little chronostratigraphic control on their evolution [*Dulanya*, 2017; *Wedmore et al.*,  
155 in prep.]. As elsewhere in the EARS [*Versfelt & Rosendahl*, 1989], these grabens follow the  
156 trend of regional foliation (Figure 2a). Thus, a range of NW-NNE striking faults have formed  
157 in southern Malawi (Figure 2b). Topographic relationships demonstrate that both NW and  
158 NNE striking faults can dip in either direction orthogonal to strike (Figure 2a). Therefore, the  
159 range of fault orientations is polymodal [*Healy et al.*, 2015]; although given the lack of  
160 accurate measurements of fault dip, we cannot be sure if the range is strictly quadrimodal  
161 (four distinct clusters) or polymodal (continuous distribution of orientations).  
162

### 163 3. Strain and stress indicators within the Malawi Rift

#### 164 3.1 Previous estimates of strain and stress within the Malawi Rift

165 At the scale of the EARS, kinematic models have been developed using a combination of  
166 earthquake slip vectors, and continuous and campaign GPS measurements [Saria *et al.*, 2014;  
167 Stamps *et al.*, 2008, 2018]. For southern Malawi, these models indicate an extension azimuth  
168 of  $086^{\circ}\pm 5^{\circ}$  relative to a fixed Nubia Plate [Saria *et al.*, 2014; Stamps *et al.*, 2018]. The  
169 current azimuth of the one continuous GPS station in southern Malawi (ZOMB) is  $072^{\circ}$   
170 (Figure 2a; Stamps *et al.*, [2018]).

171  
172 *Delvaux and Barth*, [2010] used an earthquake focal mechanisms stress inversion to derive a  
173 near Andersonian normal fault stress state for the Malawi Rift, with a sub-vertical maximum  
174 compressive principal stress ( $\sigma_1$ , 83/070) and sub-horizontal  $\sigma_3$  (06/242). This  $\sigma_3$  orientation  
175 implies NE-SW extension across the rift, in contrast to the E-W extension inferred from  
176 geodetic models [Stamps *et al.*, 2018]. Furthermore, this stress inversion predicts that NNE  
177 striking faults accommodate oblique extension (Figure 2d). However, slickensides on NNE  
178 striking faults indicate nearly pure dip-slip motion, and thus approximately NW-SE extension  
179 [Bloomfield and Garson, 1965; Chorowicz and Sorlien, 1992; Wedmore *et al.*, in prep.]. The  
180 geometry of faults from seismic reflection surveys within Lake Malawi have also been used  
181 to infer NW-SE rift extension [Mortimer *et al.*, 2007; Scott *et al.*, 1992].

#### 182 183 3.2 An updated stress inversion for the Malawi Rift

184 The discrepancy in rift extension direction when inferred from earthquake focal mechanisms,  
185 geodetic models, and fault slickensides may reflect the high azimuthal error and limited  
186 dataset (13 focal mechanism across the 900 km long rift) used in the *Delvaux and Barth*,  
187 [2010] stress inversion. We therefore update this stress field with an expanded dataset of 23  
188 focal mechanisms (Table 1, Figure 1a), which incorporates: (1) subsequent seismicity such as  
189 the 2009 Karonga [Biggs *et al.*, 2010; Hamiel *et al.*, 2012] and 2018 Nsanje earthquake  
190 sequences [U.S. Department of the Interior U.S. Geological Survey, 2018], and (2) focal  
191 mechanisms from revised bodywave modelling [Craig *et al.*, 2011], which are considered  
192 more accurate than the Global Centroid Moment Tensor solutions used in the *Delvaux and*  
193 *Barth*, [2010] inversion (Table 1). As in *Delvaux and Barth*, [2010], we use Win-Tensor  
194 (version 5.8.8, *Delvaux and Sperner*, [2003]) to perform the inversion. Here, the data are first  
195 processed using the “Right Dihedron Method” to determine the possible range of  $\sigma_1$  and  $\sigma_3$   
196 orientations [Angelier & Mechler, 1977]. This range is then refined by using “Rotational  
197 Optimisation” [Delvaux & Sperner, 2003], which seeks to reduce the misfit angle ( $\omega$ )  
198 between the earthquake slip vectors and the azimuth of maximum shear stress within the  
199 inversion. This inversion is first run for both nodal planes and then subsequently with just the  
200 plane that has the smallest misfit. Focal mechanisms were progressively filtered during the  
201 Right Dihedron Method analysis using the Counting Deviation method (*Delvaux and*  
202 *Sperner*, [2003], see supplementary information S1), and then by removing cases where  
203  $\omega > 45^{\circ}$  for both nodal planes during Rotational Optimisation.

204  
205 The revised stress field shows a slight clockwise rotation of  $\sigma_3$  to 12/070 relative to the  
206 *Delvaux and Barth*, [2010] inversion (Figure 3). This  $\sigma_3$  azimuth thus lies approximately  
207 halfway between those derived in Stress States 1 and 2 and is still inconsistent with NW  
208 trending slickensides. Notably, however, the azimuthal accuracy has been improved (from  
209  $\omega = \pm 22^{\circ}$  to  $\pm 12^{\circ}$ ). This may reflect that *Delvaux and Barth*, [2010] included all focal  
210 mechanisms in their inversion regardless of whether they were compatible with each other,

211 whilst our expanded dataset allowed a more selective approach. Stress inversions combining  
212 fault slickensides [*Chorowicz and Sorlien, 1992; Wedmore et al., in prep.*] and earthquake  
213 focal mechanisms were also attempted. However, these could not produce a reliable reduced  
214 stress tensor as either the data filtering was too severe, or the resulting stress shape ratio  
215 ( $\Phi = \sigma_2 - \sigma_3 / \sigma_1 - \sigma_3$ ) indicates an unrealistic prolate stress ellipsoid ( $\Phi = 0.04$ , *Lisle et al., [2006]*;  
216 see Supplementary Information S1). In summary, the updated stress inversions for the  
217 Malawi Rift cannot distinguish between the three stress states for southern Malawi postulated  
218 in the introduction. Hence, there is a need to consider other indicators of stress and strain  
219 within the rift, and to assess fault reactivation potential in different stress states.

220

### 221 3.3 Joint orientations

222 Figures 2 and 4 show the orientations of two steeply-dipping joint sets in southern Malawi,  
223 which strike N-S and E-W. N-S striking joints have bare surfaces and are mutually cross  
224 cutting with the E-W striking set, though tend to cut across them more commonly than vice-  
225 versa. The majority of measurements were taken within the Zomba Graben; however, the N-S  
226 and E-W sets are also observed at two locations within the Makanjira Graben (Figure 2).  
227 Joint orientations were all measured >50 m from faults and are inferred to be outside their  
228 respective damage zones.

229

230 By inferring that these joints are opening parallel to the trend of  $\sigma_3$ , it is possible to derive  
231 another estimate for its orientation within southern Malawi. To do this, we quantitatively  
232 analyse joint orientations using Kamb Contours (Figure 4a), where contours represent  
233 standard deviations away from the expected density of a random sample [*Kamb, 1959*]. This  
234 analysis finds that the trend of the highest concentration of poles to the N-S striking joint set  
235 trends  $082^\circ \pm 7^\circ$ , which is taken here as the joint-derived  $\sigma_3$  trend. This trend indicates an  
236 extension direction that is within error of the geodetically-derived extension direction for the  
237 Malawi Rift [*Saria et al., 2014; Stamps et al., 2018*]. The E-W striking joints are interpreted  
238 to reflect either: (1) an orthogonal joint set to the N-S set, and/or (2) the emplacement of E-W  
239 striking Chilwa Akaline Province dykes [*Bloomfield, 1965*]. Many of the N-S striking joints  
240 are foliation-parallel and thus may not necessarily reflect tectonic stresses [e.g. *Price, 1959*;  
241 *Engelder, 1985; Williams et al., 2018*]. However, the N-S striking joint set is also observed  
242 within isotropic rocks, and so the  $\sigma_3$  trend is not significantly changed when foliation-parallel  
243 joints are removed from the analysis ( $079^\circ \pm 8^\circ$ , Figure S4).

244

## 245 4. Fault strength in southern Malawi

246 To calculate fault reactivation potential at the southern end of the Malawi Rift, it is necessary  
247 to consider the frictional properties of its faults. We therefore selected three faults  
248 (Thyolo, Chingale Step, and Bilila-Mtakataka, Figure 2a), which: (1) encompass the range of  
249 fault orientations observed in southern Malawi, (2) have late-Quaternary fault scarps, and are  
250 therefore considered active [*Jackson and Blenkinsop, 1997; Hodge et al., 2018, 2019*;  
251 *Wedmore et al., in prep.*], and (3) are well-exposed, so it is possible to sample them for  
252 compositional analysis. The footwalls of the Chingale Step and Thyolo faults consist of  
253 intensely fractured basement, which is in contact with the hanging wall post-Miocene  
254 sediments (Figure 5; *Dulanya, [2017]*). The contact itself consists of a <1 m thick fault gouge  
255 (Figure 5). Along most of its length, the Bilila-Mtakataka fault consists of a soil-mantled  
256 scarp [*Hodge et al., 2018; Jackson & Blenkinsop, 1997*]. However, at Kasinje (Figure 2a), the  
257 fault consists of a 3 m thick unit of intensely fractured gneiss that separates footwall and  
258 hanging wall hornblende gneisses [*Hodge et al., 2018*].

259

260 To assess the composition of the fault zones, X-ray diffraction (XRD) analyses were  
 261 conducted on two samples from each of the faults: (1) a ‘country rock’ sample from the intact  
 262 protolith closest to the fault, and (2) a ‘fault rock’ sample from the faulted contact itself, i.e.  
 263 the fault gouge for the Thyolo and Chingale Step faults (Figure 5), and intensely fractured  
 264 gneiss for the Bilila-Mtakataka fault. XRD patterns were collected on powdered samples with  
 265 a Philips PW1710 Automated Powder Diffractometer using Cu-K $\alpha$  radiation at 35kV and  
 266 40mA, between 2 and 70° 2 $\theta$ , at a scan speed of 0.04 °2 $\theta$ /s. From the scans, phases were  
 267 identified using Philips PC Identify software. Using the peak areas, semi-quantitative analysis  
 268 was then performed to estimate the weight percentage of each identified phase (Table 2,  
 269 Figure S5).

270

271 For each fault, we find that the phyllosilicate content is <15% (Table 2). This is significant as  
 272 faults that are frictionally weak (fault static coefficient of friction ( $\mu_s$ )<0.4) typically contain  
 273 interconnected phyllosilicates phases that constitute >30-40% of the fault rock [Massironi *et*  
 274 *al.*, 2011; Moore & Lockner, 2004]. Thus, we infer that these faults exhibit ‘Byerlee’  
 275 frictional strengths ( $\mu_s$ ~0.6-0.8; Byerlee, [1978]), which is also consistent with the results of  
 276 deformation experiments on a suite of basement lithologies from the Malawi Rift ( $\mu_s$ =0.55-  
 277 0.80; Hellebrekers *et al.*, [in review]). There are non-systematic differences in composition  
 278 between some footwall country rock and fault rock samples (Table 2). For example, the  
 279 Chingale Step fault gouge is near pure calcite, yet this phase is not detected in its country  
 280 rock sample. These samples alone, however, are insufficient to determine if these differences  
 281 reflect local protolith variations, near-surface weathering [Isaacs *et al.*, 2007], or fault zone  
 282 alteration [*sensu* Sutherland *et al.*, 2012].

283

## 284 5. Fault reactivation potential analysis in southern Malawi

285 Fault reactivation potential considers how susceptible a fault, of a given orientation and stress  
 286 state, is to slip under the Mohr-Coulomb failure criterion. This criterion describes the shear  
 287 stress ( $\tau$ ) required for a fault to exceed its frictional resistance:

288

289

$$\tau = c + \mu_s(\sigma_n - P_f) \quad (1)$$

290

291 where  $\sigma_n$  is the normal stress,  $c$  is the cohesive strength, and  $P_f$  is pore fluid pressure. We  
 292 consider fault reactivation in potential in southern Malawi in terms of Stress Ratio, Slip  
 293 Tendency, and effective coefficient of friction (Figure 6).

294

### 295 5.1. Stress ratio

296 The stress ratio is the ratio between  $\sigma_3$  and  $\sigma_1$  required for fault slip ( $Q=\sigma_3/\sigma_1$ , Figure 6;  
 297 Sibson, [1985]). For the faults considered here, which strike obliquely to  $\sigma_3$  and do not  
 298 contain  $\sigma_2$ , we use the 3D solution outlined by Leclère and Fabbri, [2013], where:

299

300

$$Q = \frac{-(2AD\mu_s + 2C) \pm \sqrt{\Delta}}{A^2\mu_s^2 - C} \quad (2)$$

301

302 Here,  $A$ ,  $B$ ,  $C$ ,  $D$  and  $\Delta$  are functions defined by the stress shape ratio ( $\Phi$ ),  $c$ ,  $\mu_s$ , magnitude of  
 303  $\sigma_1$ , and the direction cosines between the normal to the fault plane and the three principal  
 304 stress axes (see supplementary information S2).  $Q$  and  $\mu_s$  must be real numbers with  $Q \leq 1$   
 305 and  $\mu_s \geq 0$  [Leclère & Fabbri, 2013].

306

307 We calculate  $Q$  for the three faults described in section 4, given Stress States 1 and 2. For  
 308 Stress State 1 ( $\alpha$  is  $\sim 90^\circ$  for NW-striking faults and  $\sim 40^\circ$  for NNE-striking faults) we use the  
 309 principal stress orientations derived in the *Delvaux and Barth*, [2010] stress inversion  
 310 ( $\sigma_1=83/070$ ,  $\sigma_2=02/333$ ,  $\sigma_3=06/242$ ), whilst for Stress State 2 ( $\alpha$  is  $\sim 60^\circ$  for all faults) the  
 311 principal stress orientations are based on joint orientations ( $\sigma_1=90/000$ ,  $\sigma_2=00/172$ ,  
 312  $\sigma_3=00/082$ ). No reactivation analysis is conducted for the stress rotation hypothesis (Stress  
 313 State 3), as it intrinsically assumes that all faults are optimally oriented for failure [*Morley*,  
 314 2010].

315

316 The strike of the Chingale Step and Thyolo faults is well constrained from their prominent  
 317 scarps that are visible in a 12 m resolution TanDEM-X digital elevation model [*Hodge et al.*,  
 318 2019; *Wedmore et al.*, in prep.] . For the Chingale Step fault, the strike is the orientation of  
 319 the line that connects the two ends of its scarp, whilst for the segmented Thyolo fault, strike  
 320 is the orientation of its longer north-western section (Figure 2a). The Bilila-Mtakataka fault is  
 321 best described by two sub-parallel segments, the longest of which is oriented 156/46 NE  
 322 [*Hodge et al.*, 2018]. Dips of  $57^\circ$  and  $60^\circ$  for the Chingale and Thyolo faults were derived  
 323 from field measurements (Figure 5). Although there is an uncertainty in how representative  
 324 these surface measurements of fault dip are, these measurements are similar to those inferred  
 325 at depth from geophysical surveys elsewhere in the Malawi Rift ( $45\text{--}65^\circ$ ; *Wheeler and*  
 326 *Rosendahl*, [1994]; *Mortimer et al.*, [2007]; *Kolawole et al.*, [2018]).

327

328 As justified in section 4, we infer that these faults exhibit Byerlee frictional strengths, and so  
 329 a value of  $\mu_s=0.7$  is used. A foliation-parallel pre-existing fault would generally be  
 330 considered cohesionless [*Morley et al.*, 2004; *Sibson*, 1985]. However, the high-grade  
 331 metamorphic fabrics within the Malawi Rift are qualitatively observed to be cohesive (Figure  
 332 4b). Furthermore, the low rift strain rates ( $\sim 2$  mm/yr; *Saria et al.*, [2014]) imply that there are  
 333 long recurrence intervals between earthquakes, so it is possible that interseismic healing has  
 334 led to a recovery of some fault cohesion [*Tenthorey & Cox*, 2006]. To account for this  
 335 ambiguity, we calculate  $Q$  for end-member cases where  $c=0$  and  $c=40$  MPa, the latter of  
 336 which is derived from crystalline rocks typically exhibiting tensile strengths ( $T_0$ ) of 20 MPa,  
 337 and that  $c \approx 2T_0$  [*Lockner*, 1995; *Sibson*, 1985, 1998].

338

339 No knowledge of stress magnitudes is required for calculating  $Q$  for a cohesionless fault  
 340 [*Leclère & Fabbri*, 2013]. However, the magnitude of  $\sigma_1$  is needed to determine  $Q$  for a  
 341 cohesive fault, which is calculated by assuming an Andersonian normal fault stress state  
 342 where:

343

344

$$\sigma_1 = \sigma_v = \bar{\rho}(z)gz \quad (3)$$

345

346 where  $\sigma_v$  is the vertical stress,  $g$  is gravity ( $9.8 \text{ ms}^{-2}$ ),  $z$  is depth, and  $\bar{\rho}(z)$  is the average  
 347 density of the overlying crust for a given depth, which is a function of a Malawi Rift three-  
 348 layer crustal model (Table S2; *Nyblade and Langston*, [1995]; *Fagereng*, [2013]). As  $Q$  will  
 349 vary with depth for a cohesive fault, it is calculated here between 6-35 km, which  
 350 encompasses the depth range for instrumentally-recorded earthquake nucleation in the  
 351 Malawi Rift [*Biggs et al.*, 2010; *Craig et al.*, 2011; *Nyblade & Langston*, 1995].

352

353 We assume the pore fluid pressure,  $P_f=0$ ; however, the influence of fluids on fault  
 354 reactivation is assessed in section 5.3. The stress shape ratio ( $\Phi$ ) is 0.33, as derived from the

355 updated stress inversion (Figure 3). For comparison, the orientation of the faults is shown in a  
 356 stereoplot that is contoured by  $Q$  values for a given set of  $\Phi$ ,  $\mu_s$ , principal stress orientations,  
 357 and (for cohesive faults) depth. To allow for the uncertainty in  $\Phi$  and  $\mu_s$ ,  $Q$ -contour plots are  
 358 also constructed in  $\Phi$ - $\mu_s$  space for a fixed set of fault and principal stress orientations  
 359 [Boulton *et al.*, 2018].

360

### 361 5.2 Slip tendency

362 Slip tendency ( $T_s$ ) is a measure of the ratio of  $\tau$  to  $\sigma_n$  acting on the fault surface [Lisle &  
 363 Srivastava, 2004; Morris *et al.*, 1996]:

364

$$365 \quad T_s = \frac{\tau}{\sigma_n} \quad (4)$$

366

367 For a given stress state, there is a maximum value of  $T_s$ , which is that acting on a  
 368 cohesionless optimally-oriented fault (Figure 6; Lisle and Srivastava, [2004]). This leads to  
 369 the definition of a normalized index of slip tendency ( $T'_s$ ) that ranges between 0-1:

370

$$371 \quad T'_s = \frac{T_s}{\max(T_s)} = \frac{\tau}{\sigma_n \tan \phi} \quad (5)$$

372

373 (corrected from eq. 3 in Lisle and Srivastava, [2004]; pers. comm. R. Lisle) where  $\phi$  is the  
 374 angle of internal fault friction ( $\tan \phi = \mu_s$ ). A fault with low  $T'_s$  thus also reactivates at low  $Q$   
 375 (Figure 6). To calculate  $T_s$  and  $T'_s$  for the Chingale Step, Thyolo and Bilila-Mtakataka faults  
 376 without knowledge of the magnitudes of  $\tau$  and  $\sigma_n$ , we use the solutions outlined by Lisle and  
 377 Srivastava, [2004] (see supplementary information S3). This analysis is performed for Stress  
 378 States 1 and 2, assuming  $\mu_s=0.7$ ,  $P_f=0$ , and  $\Phi = 0.33$ .

379

### 380 5.3 Fault effective coefficient of friction

381 The concept of  $T_s$  can be extended to calculate the effective coefficient of friction ( $\mu_s'$ ),  
 382 which describes the maximum value of  $\mu_s$  or lowest value of  $P_f$  that allows faults to reactivate  
 383 for a given stress state, without also inducing failure along optimally oriented planes in intact  
 384 rock (Figure 6; Sibson, [1985]; Muluneh *et al.*, [2018]). Like  $T_s$ ,  $\mu_s'$  is a measure of the ratio  
 385 of  $\tau$  to  $\sigma_n$  acting on a fault, however, it is derived using inferred principal stress magnitudes,  
 386 and fault cohesion can be incorporated. This is advantageous as  $\mu_s'$  can then be compared to  
 387 values of  $\mu_s$  inferred from experimental and compositional analysis of faults to determine if  
 388 they will reactivate in a given stress state, or if elevated fluid pressures are required for  
 389 reactivation.

390

391 Principal stress magnitudes can be derived as  $\mu_s'$  is being equated to the stresses acting on an  
 392 optimally oriented fault (Figure 6). In this case, the relative principal stress magnitudes can  
 393 be calculated using Mohr-Coulomb theory [Jaeger *et al.*, 2007]:

394

$$395 \quad \sigma_1 = 2c \sqrt{\frac{1 + \sin \phi_{intact}}{1 - \sin \phi_{intact}}} + \sigma_3 \left( \frac{1 + \sin \phi_{intact}}{1 - \sin \phi_{intact}} \right) \quad (6)$$

396

397 where  $\phi_{intact} = \tan^{-1} \mu_{s-intact}$ , and  $\mu_{s-intact}$  is the frictional strength of intact rock. Given the results  
 398 of Hellebrekers *et al.*, [in review], we take  $\mu_{s-intact}$  to equal 0.7, thus  $\phi_{intact} = 35^\circ$  and is the same

399 as the fault frictional strength ( $\mu_s$ ). Since  $\sigma_1$  can be derived from eq. 3, it is thus also possible  
 400 to calculate  $\sigma_3$  and  $\sigma_2$  by rearranging eq. 6 and the equation for  $\Phi$  (eq. S1) respectively. The  
 401 principal stress magnitudes can then be used to calculate  $\tau$  and  $\sigma_n$  as a function of depth  
 402 [Jaeger *et al.*, 2007], and  $\mu_s'$  can be derived by rearranging the Mohr Coulomb criterion (eq.  
 403 1). Thus, for the parameters assumed here:

$$404 \quad \mu_s'(z) = \frac{\sqrt{C \left( \frac{2.7z\bar{\rho}(z) - 42}{9.8z\bar{\rho}(z)} \right)^2 - 2C \left( \frac{2.7z\bar{\rho}(z) - 42}{9.8z\bar{\rho}(z)} \right) + C - \frac{c}{\sigma_1}}}{A \left( \frac{2.7z\bar{\rho}(z) - 42}{9.8z\bar{\rho}(z)} \right) + B} \quad (7)$$

406 where the functions  $A$ ,  $B$ , and  $C$  are defined by equations S2-S4 (see supplementary  
 407 information S4). As previously, we calculate  $\mu_s'$  for the Thyolo, Chingale Step, and Bilila-  
 408 Mtakataka faults being reactivated in Stress States 1 and 2 over a depth range of 6-35 km and  
 409 consider both cohesionless and cohesive faults. If  $\mu_s'$  and  $\mu_{s-intact}$  are set to be the same, then  
 410 the minimum pore fluid pressure ( $P_f'$ ) required to reactivate a fault (Figure 6) can be  
 411 calculated from  $\mu_s'$  as a function of depth:

$$412 \quad P_f(z) = \sigma_n(z) - \left( \frac{\sigma_n(z)\mu_s'(z)}{\mu_s} \right) \quad (8)$$

413 (see supplementary information S4). This is calculated with  $\mu_s=0.7$  and is plotted in terms of  
 414 the effective pore-fluid factor ( $\lambda_v'=P_f'/\sigma_v$ ). In addition, we show the results of this analysis at  
 415 a depth of 20 km in 3D Mohr Space using MohrPlotter v. 2.8.3 [Allmendinger *et al.*, 2013].  
 416  
 417  
 418

## 419 6. Fault reactivation potential results

420 The Thyolo and Bilila-Mtakataka faults have a high reactivation potential under Stress State  
 421 1, as their  $Q$  value is 'favourable' ( $Q>0.5Q_{Optimal}$ , Figures 6b and 7; Sibson, [1985]; Leclère  
 422 and Fabbri, [2013]), and  $T'_s \sim 1$  (Table 3, Figure S6). Thus, they will reactivate under Stress  
 423 State 1 at relatively high  $\mu_s'$  ( $>0.55$ ), regardless of whether they are cohesive or not (Table 3,  
 424 Figures 8 and 9a). Conversely, the Chingale Step fault is 'unfavourably' ( $0.5Q_{Optimal}>Q>0$ ;  
 425 Figures 6c and 7a) to 'severely misoriented' ( $Q<0$  Figures 6d and 7c) in this stress state,  
 426 depending on depth and whether it is cohesive or not.  $T'_s=0.67$  (Table 3), and at depths  $>10$   
 427 km, will not reactivate in Stress State 1 unless  $\mu_s'<0.7$  or  $\lambda_v'>0.1$  (Table 3, Figures 8b, 9, and  
 428 S7b).

429  
 430 In Stress State 2, all faults are favourably oriented (Figure 6b) and exhibit  $T'_s>0.8$ , although  
 431 the reactivation potentials of the Thyolo and Bilila-Mtakataka faults are slightly less than  
 432 under Stress State 1 (Table 3). In Stress State 2, all faults will reactivate at  $\mu_s>0.5$  at depths  
 433  $>10$  km (Table 3, Figures 8 and 9b). All results for  $Q$  are broadly independent of the values  
 434 of  $\Phi$  and  $\mu_s$  used in this analysis (Figures 10 and S8).  
 435

## 436 7. How do faults in southern Malawi reactivate?

437 Although the Thyolo and Bilila-Mtakataka faults are well oriented in Stress State 1, the  
 438 Chingale fault in the Zomba Graben is unfavourably to severely misoriented (Table 3). Late  
 439 Quaternary activity on this fault has been demonstrated by Wedmore *et al.*, [in prep.], and so

440 its orientation is representative of a structure currently accommodating extension in this  
441 region. To reactivate as a cohesionless fault under Stress State 1 at 10-35 km depth -the depth  
442 range at which the majority of earthquakes nucleate in the Malawi Rift (Table 1)-  $\mu_s'$  ranges  
443 between 0.5-0.7 (Figure 8b). This is at the lower end of frictional strengths inferred from its  
444 composition (Table 2) and deformation experiments on basement rocks in Malawi  
445 [Hellebrekers *et al.*, in review]. In the cohesive fault case,  $\mu_s' < 0.45$  (Figure 8b), and so below  
446 its likely frictional strength.

447  
448 Alternatively, the Chingale fault may reactivate under Stress State 1 at  $\mu_s = 0.7$  through an  
449 increase in fluid pressure ( $\lambda_v' < 0.2$ , Figure S8). These fluid pressures are sustainable in a  
450 normal fault stress state [Sibson & Rowland, 2003]. However, the crust in the Malawi Rift  
451 has been dehydrated during one or more episodes of high grade metamorphism, and is  
452 therefore likely to be comparatively dry [Fagereng, 2013]. Furthermore, where faults do host  
453 high fluid pressures, they often contain extensive vein networks [e.g. Bruhn *et al.*, 1994;  
454 Caine *et al.*, 2010; Sutherland *et al.*, 2012], which are not observed in the fault zones we  
455 considered (Figures 4b and 5).

456  
457 We emphasise that this reactivation analysis cannot definitively discount any of the possible  
458 stress states assessed here. Ideally, stress orientations would be measured using a range of  
459 techniques (e.g. borehole breakouts). Nevertheless, if we assume frictionally strong faults and  
460 cohesive high grade metamorphic fabrics, then it is difficult to account for why a structure  
461 with the NNE-SSW strike of the Chingale Step fault (or indeed other similarly-oriented faults  
462 in the Zomba Graben, Figure 2a) would have activated and continue reactivating in Stress  
463 State 1, instead of a more optimally oriented fault forming. Conversely, all faults are  
464 favourably oriented in Stress State 2, and so can reactivate at  $\mu_s$  or  $P_f$  that require neither  
465 frictionally weak minerals nor elevated fluid pressure (Figure 8). Furthermore, this stress  
466 state is consistent with joint orientations and the geodetically-derived extension direction  
467 [Stamps *et al.*, 2018].

468  
469 Under the Wallace-Bott criterion, southern Malawi accommodates NE-SW extension in  
470 Stress State 1 (Figure 2d) or E-W extension in Stress State 2. It is thus difficult to reconcile  
471 these stress states to the range of NW-SE to NE-SW extension directions have been proposed  
472 (see Section 3.1). Notably, however, fault slickensides and earthquake focal mechanisms in  
473 the Zomba Graben (Table 1, Figure 5; Chorowicz and Sorlien, [1992]; Wedmore *et al.*, in  
474 [prep.]) indicate NW-SE extension, in contrast to the highly oblique ( $\alpha < 40^\circ$ ) NE-SW  
475 extension predicted by applying the Wallace-Bott criterion to Stress State 1.

476  
477 A range of extension directions can be accounted for by the model proposed in Morley,  
478 [2010] where pre-existing Southern Irumide metamorphic fabrics rotate  $\sigma_3$  along the southern  
479 Malawi rift, so that all faults are pure dip-slip (i.e. Stress State 3, Figure 2f). In this way, all  
480 faults will be optimally oriented for reactivation. Furthermore, although some oblique-slip  
481 focal mechanisms (Table 1) and fault slickensides (Figure S2) are recorded in southern  
482 Malawi, in the former case, these tend to be historical focal mechanisms that were not  
483 instrumentally well-recorded, whilst with regards to the latter, this may relate to slickensides  
484 that record the inherent oblique slip component of normal faulting earthquakes as the fault tip  
485 is approached [Hampel *et al.*, 2013; Philippon *et al.*, 2015]. There is, however, a discrepancy  
486 between this hypothesis and the homogenous orientation of joint sets in southern Malawi  
487 Rift, which suggest a uniform stress state (Figure 2 and 4). The Bilila Mtakataka and  
488 Chingale Step faults also locally cross-cut the foliation in a non-systematic manner at the

489 surface (Figure 2a; *Bloomfield*, [1965]; *Jackson and Blenkinsop*, [1997]; *Hodge et al.*,  
 490 [2018]), further suggesting that the foliation is not actively rotating stresses.

491  
 492 We therefore propose a variation of the *Morley*, [2010] hypothesis based on analogue models  
 493 [*Corti et al.*, 2013; *Philippon et al.*, 2015]. Here, the regional principal stress axes [*sensu*  
 494 *Pollard et al.*, 1993] in southern Malawi are uniformly parallel to those in Stress State 2,  
 495 however, at the local scale [*sensu Twiss and Unruh*, 1998] fault slip vectors are rotated to  
 496 dip-slip along the rift by a deep-seated weak ductile shear zone that is oblique to  $\sigma_3$ , but  
 497 which conditions the geometry and distribution of the rift's faults (Figure 2e; *Hodge et al.*,  
 498 [2018]; *Wedmore et al.*, [in prep.]; Figure 2e). The following constraints are therefore  
 499 satisfied: (1) frictionally strong normal faults with a wide range of strikes are reactivated, (2)  
 500 consistently oriented sets of N-S and E-W striking joints, (3) all faults have dip-slip  
 501 kinematics. If true, this hypothesis has the following implications:

- 502
- 503 • A polymodal range of fault orientations at the southern end of the Malawi Rift (Figure  
 504 2a) can be accounted for by a uniform stress state and the Mohr Coulomb criterion,  
 505 given that  $\Phi$  is low and variably oriented pre-existing crustal weaknesses [c.f. *Healy*  
 506 *et al.*, 2015].
- 507 • Unlike in other rifts, variably striking faults in southern Malawi do not reactivate with  
 508 faults striking orthogonally to  $\sigma_3$  being linked by faults striking highly obliquely to  
 509  $\sigma_3$ . Instead, all faults can reactivate while striking slightly oblique to a uniformly E-W  
 510 trending  $\sigma_3$  (Figure 2e).
- 511 • Using fault slickensides and earthquake focal mechanisms in stress inversions is  
 512 problematic as regional stresses and fault displacement are not necessarily aligned  
 513 [*Philippon et al.*, 2015; *Twiss & Unruh*, 1998]. Furthermore, accurate principal stress  
 514 directions will not be derived from stress inversions in which only a subset of fault  
 515 orientations from a polymodal distribution are included [*Healy et al.*, 2015; *Twiss &*  
 516 *Unruh*, 1998].
- 517 • This justifies a reassessment of the stress states and extension directions that have  
 518 been inferred elsewhere in the Malawi Rift [*Chorowicz & Sorlien*, 1992; *Delvaux &*  
 519 *Barth*, 2010; *Mortimer et al.*, 2007; *Ring et al.*, 1992], and other rifts where highly-  
 520 oblique transfer zones have been proposed [e.g. *Chorowicz and Deffontaines*, 1993;  
 521 *Acocella et al.*, 1999].
- 522 • Normal faults with a wide range of strikes can all reactive within the same stress state,  
 523 which should be considered during seismic hazard assessment of continental rifts.
- 524

## 525 8. Conclusions

526 Attempts to determine the stress state in the Malawi Rift using fault geometry and  
 527 slickensides [*Chorowicz & Sorlien*, 1992; *Mortimer et al.*, 2007; *Scott et al.*, 1992],  
 528 earthquake focal mechanisms (Figure 3, *Delvaux and Barth*, [2010]), and geodetic models  
 529 [*Saria et al.*, 2014; *Stamps et al.*, 2018] have produced ambiguous results. Therefore, to test  
 530 the applicability of two possible stress states, we determined the reactivation potential of  
 531 three representative differently-oriented faults in southern Malawi, in terms of their slip  
 532 tendency, stress ratio, and effective coefficient of friction. The NW-SE striking Thyolo and  
 533 Bilila-Mtakataka faults are well-oriented with respect to a stress state where  $\sigma_3$  is SW  
 534 trending (Stress State 1, Figure 2d). However, it is difficult to account for the reactivation of  
 535 the unfavourably to severely misoriented NNE-SSW striking Chingale Step fault under Stress  
 536 State 1, given realistic frictional properties of the rift ( $\mu_s \sim 0.7$ ,  $P_f \sim 0$ ). If  $\sigma_3$  has a consistent

537 ~E-W trend (Stress State 2, Figure 2e), all faults are favourably oriented to reactivate. An  
 538 alternative hypothesis that fabrics actively rotate the stresses along the rift (Stress State 3,  
 539 Figure 2f; *Morley*, [2010]), is inconsistent with spatially homogeneous joint orientations and  
 540 local variations in the foliation orientation.

541  
 542 From this reactivation analysis, we consider that Stress State 2 is most applicable to southern  
 543 Malawi, which is also consistent with regional joint sets (Figures 2 and 4) and large scale  
 544 geodetic models [*Stamps et al.*, 2018]. This would suggest that all faults in southern Malawi  
 545 reactivate by being slightly oblique (angle between fault strike and regional  $\sigma_3$  trend  $<30^\circ$ ),  
 546 and thus counter to typical models of oblique rifting in which one fault set strikes orthogonal  
 547 to  $\sigma_3$  and the other is highly oblique [*Acocella et al.*, 1999; *Bellahsen & Daniel*, 2005;  
 548 *McClay & White*, 1995].

549  
 550 It is unclear whether the slightly oblique E-W extension predicted by Stress State 2 in  
 551 southern Malawi is reflected in the fault's kinematics, or if the faults are actually pure dip-  
 552 slip as indicated by the few well-determined focal mechanisms (Table 1). In the latter case,  
 553 this inconsistency can be explained by a deep-seated zone of crustal weakness, which is  
 554 exploited by the rift's faults and re-orient slip [*Corti et al.*, 2013; *Hodge et al.*, 2018;  
 555 *Philippon et al.*, 2015]. Nevertheless, in rifts where stress states derived from measurements  
 556 of fault displacement are ambiguous, fault reactivation potential analysis provides a powerful  
 557 way to test their applicability.

558

## 559 **Acknowledgements**

560 This research was funded by EPSRC Global Challenges Research Fund (grant number  
 561 EP/P028233/1 'PREPARE'). Henri Leclère and Carolyn Boulton are thanked for providing  
 562 codes to calculate the stress ratio of faults and guidance on how to use them. Antony Oldroyd  
 563 conducted the XRD analysis and interpretation. All data is available from the corresponding  
 564 author on request.

565

## 566 **References**

- 567 Acocella, V., Faccenna, C., Funicello, R., & Rossetti, F. (1999). Sand-box modelling of  
 568 basement-controlled transfer zones in extensional domains. *Terra Nova*.  
 569 <https://doi.org/10.1046/j.1365-3121.1999.00238.x>
- 570 Aldrich, M. J. (1986). Tectonics of the Jemez lineament in the Jemez Mountains and Rio  
 571 Grande Rift ( USA). *Journal of Geophysical Research*.  
 572 <https://doi.org/10.1029/JB091iB02p01753>
- 573 Allmendinger, R. W., Cardozo, N. C., & Fisher, D. (2013). *Structural Geology Algorithms:  
 574 Vectors & Tensors*. Cambridge University Press, Cambridge, England.
- 575 Andreoli, M. A. G. (1984). Petrochemistry, tectonic evolution and metasomatic  
 576 mineralisations of Mozambique belt granulites from S Malawi and Tete (Mozambique).  
 577 *Precambrian Research*, 25(1–3), 161–186. [https://doi.org/10.1016/0301-  
 578 9268\(84\)90031-7](https://doi.org/10.1016/0301-9268(84)90031-7)
- 579 Angelier, J., & Mechler, P. (1977). Sur une méthode graphique de recherche des contraintes  
 580 principales également utilisable en tectonique et en séismologie: La méthode des dièdres  
 581 droits. *Bulletin de La Société Géologique de France*, 7(6), 1309–1318.  
 582 <https://doi.org/10.2113/gssgfbull.S7-XIX.6.1309>
- 583 Bellahsen, N., & Daniel, J. M. (2005). Fault reactivation control on normal fault growth: An

- 584 experimental study. *Journal of Structural Geology*.  
 585 <https://doi.org/10.1016/j.jsg.2004.12.003>
- 586 Bellahsen, N., Fournier, M., D'Acromont, E., Leroy, S., & Daniel, J. M. (2006). Fault  
 587 reactivation and rift localization: Northeastern Gulf of Aden margin. *Tectonics*.  
 588 <https://doi.org/10.1029/2004TC001626>
- 589 Biggs, J., Nissen, E., Craig, T., Jackson, J., & Robinson, D. P. (2010). Breaking up the  
 590 hanging wall of a rift-border fault: The 2009 Karonga earthquakes, Malawi. *Geophysical*  
 591 *Research Letters*, 37(11). <https://doi.org/10.1029/2010GL043179>
- 592 Bloomfield, K. (1958). The geology of the Port Herald Area. *Bulletin of the Geological*  
 593 *Survey, Malawi*, 9.
- 594 Bloomfield, K. (1965). The Geology of the Zomba Area. *Bulletin of the Geological Survey,*  
 595 *Malawi*, 16.
- 596 Bloomfield, K., & Garson, M. S. (1965). The Geology of the Kirk Range-Lisungwe Valley  
 597 Area. *Bulletin of the Geological Survey, Malawi*, 17.
- 598 Bott, M. H. P. (1959). The mechanics of oblique slip faulting. *Geological Magazine*, 96(2),  
 599 109–117.
- 600 Boulton, C., Barth, N. C., Moore, D. E., Lockner, D. A., Townend, J., & Faulkner, D. R.  
 601 (2018). Frictional properties and 3-D stress analysis of the southern Alpine Fault, New  
 602 Zealand. *Journal of Structural Geology*, 114, 43–54.  
 603 <https://doi.org/10.1016/j.jsg.2018.06.003>
- 604 Bruhn, R. L., Parry, W. T., Yonkee, W. a, & Thompson, T. (1994). Fracturing and  
 605 hydrothermal alteration in normal fault zones. *Pure and Applied Geophysics*, 142(3),  
 606 609–644. <https://doi.org/10.1007/BF00876057>
- 607 Brune, S., Williams, S. E., & Müller, R. D. (2018). Oblique rifting: the rule, not the  
 608 exception. *Solid Earth*, 9(5), 1187–1206. <https://doi.org/10.5194/se-2018-63>
- 609 Byerlee, J. (1978). Friction of rocks. *Pure and Applied Geophysics PAGEOPH*, 116(4–5),  
 610 615–626. <https://doi.org/10.1007/BF00876528>
- 611 Caine, J. S., Bruhn, R. L., & Forster, C. B. (2010). Internal structure, fault rocks, and  
 612 inferences regarding deformation, fluid flow, and mineralization in the seismogenic  
 613 Stillwater normal fault, Dixie Valley, Nevada. *Journal of Structural Geology*, 32(11),  
 614 1576–1589. <https://doi.org/10.1016/j.jsg.2010.03.004>
- 615 Castaing, C. (1991). Post-Pan-African tectonic evolution of South Malawi in relation to the  
 616 Karroo and recent East African rift systems. *Tectonophysics*, 191(1–2), 55–73.  
 617 [https://doi.org/10.1016/0040-1951\(91\)90232-H](https://doi.org/10.1016/0040-1951(91)90232-H)
- 618 Chorowicz, J., & Deffontaines, B. (1993). Transfer faults and pull-apart model in the  
 619 rhinegraben from analysis of multisource data. *Journal of Geophysical Research*.  
 620 <https://doi.org/10.1029/93JB00190>
- 621 Chorowicz, J., & Sorlien, C. (1992). Oblique extensional tectonics in the Malawi Rift, Africa.  
 622 *Geological Society of America Bulletin*, 104(8), 1015–1023.  
 623 [https://doi.org/10.1130/0016-7606\(1992\)104<1015:OETITM>2.3.CO;2](https://doi.org/10.1130/0016-7606(1992)104<1015:OETITM>2.3.CO;2)
- 624 Corti, G. (2012). Evolution and characteristics of continental rifting: Analog modeling-  
 625 inspired view and comparison with examples from the East African Rift System.  
 626 *Tectonophysics*. <https://doi.org/10.1016/j.tecto.2011.06.010>
- 627 Corti, G., Philippon, M., Sani, F., Keir, D., & Kidane, T. (2013). Re-orientation of the  
 628 extension direction and pure extensional faulting at oblique rift margins: Comparison  
 629 between the Main Ethiopian Rift and laboratory experiments. *Terra Nova*, 25(5), 396–  
 630 404. <https://doi.org/10.1111/ter.12049>
- 631 Craig, T. J., Jackson, J. A., Priestley, K., & Mckenzie, D. (2011). Earthquake distribution  
 632 patterns in Africa: Their relationship to variations in lithospheric and geological  
 633 structure, and their rheological implications. *Geophysical Journal International*, 185(1),

- 634 403–434. <https://doi.org/10.1111/j.1365-246X.2011.04950.x>
- 635 Delvaux, D. (2001). Tectonic and palaeostress evolution of the Tanganyika-Rukwa-Malawi  
636 rift segment, East African Rift System. *Peri-Tethys Memoir 6: Peri-Tethyan*  
637 *Rift/Wrench Basins and Passive Margins*, 545–567.
- 638 Delvaux, D., & Barth, A. (2010). African stress pattern from formal inversion of focal  
639 mechanism data. *Tectonophysics*, 482(1–4), 105–128.  
640 <https://doi.org/10.1016/j.tecto.2009.05.009>
- 641 Delvaux, D., & Sperner, B. (2003). New aspects of tectonic stress inversion with reference to  
642 the TENSOR program. *Geological Society, London, Special Publications*, 212(1), 75–  
643 100. <https://doi.org/10.1144/GSL.SP.2003.212.01.06>
- 644 Dulanya, Z. (2017). A review of the geomorphotectonic evolution of the south Malawi rift.  
645 *Journal of African Earth Sciences*. <https://doi.org/10.1016/j.jafrearsci.2017.02.016>
- 646 Ebinger, C. J. (1989). Tectonic development of the western branch of the East African rift  
647 system. *Geological Society of America Bulletin*. [https://doi.org/10.1130/0016-](https://doi.org/10.1130/0016-7606(1989)101<0885:TDOTWB>2.3.CO;2)  
648 [7606\(1989\)101<0885:TDOTWB>2.3.CO;2](https://doi.org/10.1130/0016-7606(1989)101<0885:TDOTWB>2.3.CO;2)
- 649 Ebinger, C. J., Rosendahl, B. R., & Reynolds, D. J. (1987). Tectonic model of the Malawi  
650 rift, Africa. *Tectonophysics*, 141(1–3), 215–235. [https://doi.org/10.1016/0040-](https://doi.org/10.1016/0040-1951(87)90187-9)  
651 [1951\(87\)90187-9](https://doi.org/10.1016/0040-1951(87)90187-9)
- 652 Ebinger, C. J., Deino, A. L., Tesha, A. L., Becker, T., & Ring, U. (1993). Tectonic Controls  
653 on Rift Basin Morphology: Evolution of the Northern Malawi (Nyasa) Rift. *Journal of*  
654 *Geophysical Research*, 98(B10), 17821–17836. <https://doi.org/10.1029/93jb01392>
- 655 Engelder, T. (1985). Loading paths to joint propagation during a tectonic cycle: an example  
656 from the Appalachian Plateau, U.S.A. *Journal of Structural Geology*, 7(3–4), 459–476.  
657 [https://doi.org/10.1016/0191-8141\(85\)90049-5](https://doi.org/10.1016/0191-8141(85)90049-5)
- 658 Etheridge, M. A. (1986). On the reactivation of extensional fault systems. *Philosophical*  
659 *Transactions - Royal Society of London, Series A*. <https://doi.org/10.1098/rsta.1986.0031>
- 660 Fagereng, Å. (2013). Fault segmentation, deep rift earthquakes and crustal rheology: Insights  
661 from the 2009 Karonga sequence and seismicity in the Rukwa-Malawi rift zone.  
662 *Tectonophysics*, 601, 216–225. <https://doi.org/10.1016/j.tecto.2013.05.012>
- 663 Flannery, J. W., & Rosendahl, B. R. (1990). The seismic stratigraphy of Lake Malawi,  
664 Africa: implications for interpreting geological processes in lacustrine rifts. *Journal of*  
665 *African Earth Sciences*, 10(3), 519–548. [https://doi.org/10.1016/0899-5362\(90\)90104-M](https://doi.org/10.1016/0899-5362(90)90104-M)
- 666 Fritz, H., Abdelsalam, M., Ali, K. A., Bingen, B., Collins, A. S., Fowler, A. R., et al. (2013).  
667 Orogen styles in the East African Orogen: A review of the Neoproterozoic to Cambrian  
668 tectonic evolution. *Journal of African Earth Sciences*.  
669 <https://doi.org/10.1016/j.jafrearsci.2013.06.004>
- 670 Habgood, F. (1963). The geology of the country west of the Shire River between Chikwaw  
671 and Chiromo. *Bulletin of the Geological Survey, Malawi*, 14.
- 672 Habgood, F., Holt, D. N., & Walshaw, R. D. (1973). The geology of the Thyolo Area.  
673 *Bulletin of the Geological Survey, Malawi*, 22.
- 674 Hamiel, Y., Baer, G., Kalindekaffe, L., Dombola, K., & Chindandali, P. (2012). Seismic and  
675 aseismic slip evolution and deformation associated with the 2009–2010 northern Malawi  
676 earthquake swarm, East African Rift. *Geophysical Journal International*, 191(3), 898–  
677 908. <https://doi.org/10.1111/j.1365-246X.2012.05673.x>
- 678 Hampel, A., Li, T., & Maniatis, G. (2013). Contrasting strike-slip motions on thrust and  
679 normal faults: Implications for space-geodetic monitoring of surface deformation.  
680 *Geology*. <https://doi.org/10.1130/G33927.1>
- 681 Hargrove, U. S., Hanson, R. E., Martin, M. W., Blenkinsop, T. G., Bowering, S. A., Walker,  
682 N., & Munyanyiwa, H. (2003). Tectonic evolution of the Zambezi orogenic belt:  
683 Geochronological, structural, and petrological constraints from northern Zimbabwe.

- 684 *Precambrian Research*. [https://doi.org/10.1016/S0301-9268\(03\)00066-4](https://doi.org/10.1016/S0301-9268(03)00066-4)
- 685 Healy, D., Blenkinsop, T. G., Timms, N. E., Meredith, P. G., Mitchell, T. M., & Cooke, M.  
686 L. (2015). Polymodal faulting: Time for a new angle on shear failure. *Journal of*  
687 *Structural Geology*. <https://doi.org/10.1016/j.jsg.2015.08.013>
- 688 Hellebrekers, N., Niemeijer, A., Fagereng, Å., Manda, B., & Mvula, R. (9999). Lower crustal  
689 earthquakes in the East African Rift System: Insights from frictional properties of rock  
690 samples from the Malawi Rift.
- 691 Henstra, G. A., Rotevatn, A., Gawthorpe, R. L., & Ravnås, R. (2015). Evolution of a major  
692 segmented normal fault during multiphase rifting: The origin of plan-view zigzag  
693 geometry. *Journal of Structural Geology*, *74*, 45–63.  
694 <https://doi.org/10.1016/j.jsg.2015.02.005>
- 695 Hodge, M., Fagereng, Biggs, J., & Mdala, H. (2018). Controls on Early-Rift Geometry: New  
696 Perspectives From the Bilila-Mtakataka Fault, Malawi. *Geophysical Research Letters*,  
697 *45*(9), 3896–3905. <https://doi.org/10.1029/2018GL077343>
- 698 Hodge, M., Biggs, J., Fagereng, Å., Elliott, A., Mdala, H., & Mphepo, F. (2019). A semi-  
699 automated algorithm to quantify scarp morphology (SPARTA): application to normal  
700 faults in southern Malawi. *Solid Earth*, *10*(1), 27–57.
- 701 Isaacs, A. J., Evans, J. P., Song, S.-R., & Kolesar, P. T. (2007). Structural, Mineralogical, and  
702 Geochemical Characterization of the Chelungpu Thrust Fault, Taiwan. *Terrestrial,*  
703 *Atmospheric and Oceanic Sciences*, *18*(2), 183.  
704 [https://doi.org/10.3319/TAO.2007.18.2.183\(TCDP\)](https://doi.org/10.3319/TAO.2007.18.2.183(TCDP))
- 705 Jackson, J., & Blenkinsop, T. (1997). The Bilila-Mtakataka fault in Malawi: an active, 100-  
706 km long, normal fault segment in thick seismogenic crust. *Tectonics*, *16*(1), 137–150.  
707 <https://doi.org/10.1029/96TC02494>
- 708 Jaeger, J. C., Cook, N. G., & Zimmerman, R. (2007). *Fundamentals of Rock Mechanics, 4th*  
709 *edition*. Wiley-Blackwell.
- 710 Johnson, S. P., De Waele, B., & Liyungu, K. A. (2006). U-Pb sensitive high-resolution ion  
711 microprobe (SHRIMP) zircon geochronology of granitoid rocks in eastern Zambia:  
712 Terrane subdivision of the Mesoproterozoic Southern Irumide Belt. *Tectonics*, *25*(6).  
713 <https://doi.org/10.1029/2006TC001977>
- 714 Kamb, W. B. (1959). Ice petrofabric observations from Blue Glacier, Washington, in relation  
715 to theory and experiment. *Journal of Geophysical Research*, *64*(11), 1891.  
716 <https://doi.org/10.1029/JZ064i011p01891>
- 717 Kolawole, F., Atekwana, E. A., Laó-Dávila, D. A., Abdelsalam, M. G., Chindandali, P. R.,  
718 Salima, J., & Kalindekafe, L. (2018). Active Deformation of Malawi Rift's North Basin  
719 Hinge Zone Modulated by Reactivation of Preexisting Precambrian Shear Zone Fabric.  
720 *Tectonics*, *37*(3), 683–704. <https://doi.org/10.1002/2017TC004628>
- 721 Kröner, A., Willner, A. P., Hegner, E., Jaeckel, P., & Nemchin, A. (2001). Single zircon  
722 ages, PT evolution and Nd isotopic systematics of high-grade gneisses in southern  
723 Malawi and their bearing on the evolution of the Mozambique belt in southeastern  
724 Africa. *Precambrian Research*, *109*(3–4), 257–291. [https://doi.org/10.1016/S0301-](https://doi.org/10.1016/S0301-9268(01)00150-4)  
725 [9268\(01\)00150-4](https://doi.org/10.1016/S0301-9268(01)00150-4)
- 726 Laó-Dávila, D. A., Al-Salmi, H. S., Abdelsalam, M. G., & Atekwana, E. A. (2015).  
727 Hierarchical segmentation of the Malawi Rift: The influence of inherited lithospheric  
728 heterogeneity and kinematics in the evolution of continental rifts. *Tectonics*, *34*(12),  
729 2399–2417. <https://doi.org/10.1002/2015TC003953>
- 730 Leclère, H., & Fabbri, O. (2013). A new three-dimensional method of fault reactivation  
731 analysis. *Journal of Structural Geology*, *48*, 153–161.  
732 <https://doi.org/10.1016/j.jsg.2012.11.004>
- 733 Lisle, R. J., & Srivastava, D. C. (2004). Test of the frictional reactivation theory for faults

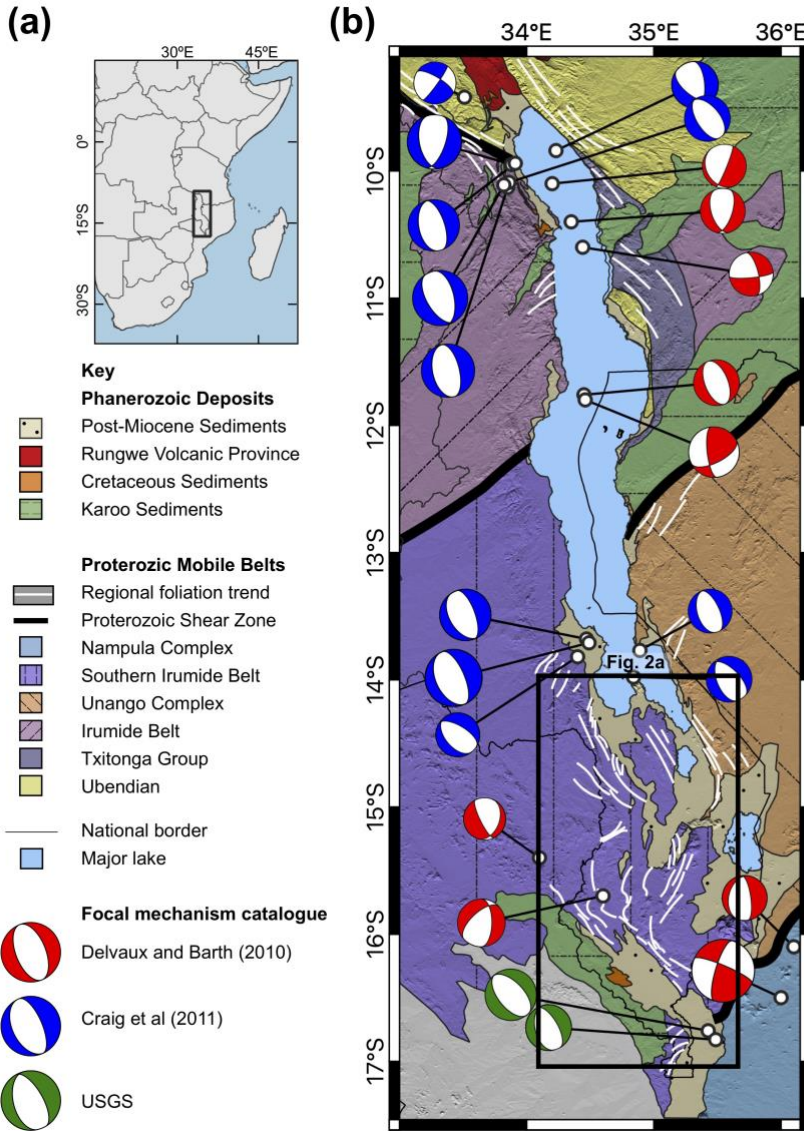
- 734 and validity of fault-slip analysis. *Geology*. <https://doi.org/10.1130/G20408.1>
- 735 Lisle, R. J., Orife, T. O., Arlegui, L., Liesa, C., & Srivastava, D. C. (2006). Favoured states of  
736 palaeostress in the Earth's crust: evidence from fault-slip data. *Journal of Structural*  
737 *Geology*, 28(6), 1051–1066. <https://doi.org/10.1016/j.jsg.2006.03.012>
- 738 Lockner, D. A. (1995). Rock failure. *Rock Physics and Phase Relations: A Handbook of*  
739 *Physical Constants*, 3, 127–147.
- 740 Lopes Cardozo, G. G. O., & Behrmann, J. H. (2006). Kinematic analysis of the Upper Rhine  
741 Graben boundary fault system. *Journal of Structural Geology*.  
742 <https://doi.org/10.1016/j.jsg.2006.03.010>
- 743 Massironi, M., Bistacchi, A., & Menegon, L. (2011). Misoriented faults in exhumed  
744 metamorphic complexes: Rule or exception? *Earth and Planetary Science Letters*,  
745 307(1–2), 233–239. <https://doi.org/10.1016/j.epsl.2011.04.041>
- 746 McClay, K. R., & White, M. J. (1995). Analogue modelling of orthogonal and oblique rifting.  
747 *Marine and Petroleum Geology*. [https://doi.org/10.1016/0264-8172\(95\)92835-K](https://doi.org/10.1016/0264-8172(95)92835-K)
- 748 Moore, D. E., & Lockner, D. a. (2004). Crystallographic controls on the frictional behavior of  
749 dry and water-saturated sheet structure minerals. *Journal of Geophysical Research*,  
750 109(B03401), 1–16. <https://doi.org/10.1029/2003JB002582>
- 751 Morley, C. K. (2010). Stress re-orientation along zones of weak fabrics in rifts: An  
752 explanation for pure extension in “oblique” rift segments? *Earth and Planetary Science*  
753 *Letters*, 297(3–4), 667–673. <https://doi.org/10.1016/j.epsl.2010.07.022>
- 754 Morley, C. K., Haranya, C., Phoosongsee, W., Pongwapee, S., Kornawan, A., & Wonganan,  
755 N. (2004). Activation of rift oblique and rift parallel pre-existing fabrics during  
756 extension and their effect on deformation style: Examples from the rifts of Thailand.  
757 *Journal of Structural Geology*, 26(10), 1803–1829.  
758 <https://doi.org/10.1016/j.jsg.2004.02.014>
- 759 Morris, A., Ferrill, D. A., & Henderson, D. B. (1996). Slip-tendency analysis and fault  
760 reactivation. *Geology*. [https://doi.org/10.1130/0091-](https://doi.org/10.1130/0091-7613(1996)024<0275:STAAFR>2.3.CO;2)  
761 [7613\(1996\)024<0275:STAAFR>2.3.CO;2](https://doi.org/10.1130/0091-7613(1996)024<0275:STAAFR>2.3.CO;2)
- 762 Mortimer, E. J., Paton, D. A., Scholz, C. A., Strecker, M. R., & Blisniuk, P. (2007).  
763 Orthogonal to oblique rifting: Effect of rift basin orientation in the evolution of the  
764 North basin, Malawi Rift, East Africa. *Basin Research*, 19(3), 393–407.  
765 <https://doi.org/10.1111/j.1365-2117.2007.00332.x>
- 766 Mortimer, E. J., Kirstein, L. A., Stuart, F. M., & Strecker, M. R. (2016). Spatio-temporal  
767 trends in normal-fault segmentation recorded by low-temperature thermochronology:  
768 Livingstone fault scarp, Malawi Rift, East African Rift System. *Earth and Planetary*  
769 *Science Letters*, 455, 62–72. <https://doi.org/10.1016/j.epsl.2016.08.040>
- 770 Mulneh, A. A., Kidane, T., Corti, G., & Keir, D. (2018). Constraints on fault and crustal  
771 strength of the Main Ethiopian Rift from formal inversion of earthquake focal  
772 mechanism data. *Tectonophysics*, 731–732, 172–180.  
773 <https://doi.org/10.1016/j.tecto.2018.03.010>
- 774 Nyblade, A. A., & Langston, C. A. (1995). East African earthquakes below 20 km depth and  
775 their implications for crustal structure. *Geophysical Journal International*, 121(1), 49–  
776 62. <https://doi.org/10.1111/j.1365-246X.1995.tb03510.x>
- 777 Petit, C., Déverchère, J., Houdry, F., Sankov, V. A., Melnikova, V. I., & Delvaux, D. (1996).  
778 Present-day stress field changes along the Baikal rift and tectonic implications.  
779 *Tectonics*, 15(6), 1171–1191. <https://doi.org/10.1029/96TC00624>
- 780 Philippon, M., Willingshofer, E., Sokoutis, D., Corti, G., Sani, F., Bonini, M., & Cloetingh,  
781 S. (2015). Slip re-orientation in oblique rifts. *Geology*, 43(2), 147–150.  
782 <https://doi.org/10.1130/G36208.1>
- 783 Pollard, D. D., Saltzer, S. D., & Rubin, A. M. (1993). Stress inversion methods: are they

- 784 based on faulty assumptions? *Journal of Structural Geology*.  
 785 [https://doi.org/10.1016/0191-8141\(93\)90176-B](https://doi.org/10.1016/0191-8141(93)90176-B)
- 786 Price, N. J. (1959). Mechanics of jointing in rocks. *Geological Magazine*, 96(2), 149–167.  
 787 <https://doi.org/10.1017/S0016756800060040>
- 788 Ring, U., Betzler, C., & Delvaux, D. (1992). Normal vs. strike-slip faulting during rift  
 789 development in East Africa: The Malawi rift. *Geology*, 20(11), 1015–1018.  
 790 [https://doi.org/10.1130/0091-7613\(1992\)020<1015:NVSSFD>2.3.CO;2](https://doi.org/10.1130/0091-7613(1992)020<1015:NVSSFD>2.3.CO;2)
- 791 Roberts, E. M., Stevens, N. J., O'Connor, P. M., Dirks, P. H. G. M., Gottfried, M. D., Clyde,  
 792 W. C., et al. (2012). Initiation of the western branch of the East African Rift coeval with  
 793 the eastern branch. *Nature Geoscience*, 5(4), 289–294. <https://doi.org/10.1038/ngeo1432>
- 794 Sandwell, D., Mellors, R., Tong, X., Wei, M., & Wessel, P. (2011). Open radar  
 795 interferometry software for mapping surface Deformation. *Eos, Transactions American*  
 796 *Geophysical Union*. <https://doi.org/10.1029/2011EO280002>
- 797 Saria, E., Calais, E., Stamps, D. S., Delvaux, D., & Hartnady, C. J. H. (2014). Present-day  
 798 kinematics of the East African Rift. *Journal of Geophysical Research: Solid Earth*,  
 799 119(4), 3584–3600. <https://doi.org/10.1002/2013JB010901>
- 800 Scott, D. L., Etheridge, M. A., & Rosendahl, B. R. (1992). Oblique-slip deformation in  
 801 extensional terrains: A case study of the lakes Tanganyika and Malawi Rift Zones.  
 802 *Tectonics*. <https://doi.org/10.1029/92TC00821>
- 803 Sibson, R. H. (1985). A note on fault reactivation. *Journal of Structural Geology*, 7(6), 751–  
 804 754. [https://doi.org/10.1016/0191-8141\(85\)90150-6](https://doi.org/10.1016/0191-8141(85)90150-6)
- 805 Sibson, R. H. (1998). Brittle failure mode plots for compressional and extensional tectonic  
 806 regimes. *Journal of Structural Geology*, 20(5), 655–660. [https://doi.org/10.1016/S0191-8141\(98\)00116-3](https://doi.org/10.1016/S0191-8141(98)00116-3)
- 808 Sibson, R. H., & Rowland, J. V. (2003). Stress, fluid pressure and structural permeability in  
 809 seismogenic crust, North Island, New Zealand. *Geophysical Journal International*,  
 810 154(2), 584–594. <https://doi.org/10.1046/j.1365-246X.2003.01965.x>
- 811 Stamps, D. S., Calais, E., Saria, E., Hartnady, C., Nocquet, J. M., Ebinger, C. J., &  
 812 Fernandes, R. M. (2008). A kinematic model for the East African Rift. *Geophysical*  
 813 *Research Letters*, 35(5). <https://doi.org/10.1029/2007GL032781>
- 814 Stamps, D. S., Saria, E., & Kreemer, C. (2018). A Geodetic Strain Rate Model for the East  
 815 African Rift System. *Scientific Reports*. <https://doi.org/10.1038/s41598-017-19097-w>
- 816 Sutherland, R., Toy, V. G., Townend, J., Cox, S. C., Eccles, J. D., Faulkner, D. R., et al.  
 817 (2012). Drilling reveals fluid control on architecture and rupture of the Alpine fault,  
 818 New Zealand. *Geology*, 40(12), 1143–1146. <https://doi.org/10.1130/G33614.1>
- 819 Tenthorey, E., & Cox, S. F. (2006). Cohesive strengthening of fault zones during the  
 820 interseismic period: An experimental study. *Journal of Geophysical Research: Solid*  
 821 *Earth*, 111(9). <https://doi.org/10.1029/2005JB004122>
- 822 Twiss, R. J., & Unruh, J. R. (1998). Analysis of fault slip inversions: Do they constrain stress  
 823 or strain rate? *Journal of Geophysical Research: Solid Earth*.  
 824 <https://doi.org/10.1029/98JB00612>
- 825 U.S. Department of the Interior U.S. Geological Survey. (2018). M 5.5 - 24km NE of Nsanje,  
 826 Malawi [available at  
 827 <https://earthquake.usgs.gov/earthquakes/eventpage/us1000d1cy#executive>, last accessed  
 828 26 Sept 2018].
- 829 Versfelt, J., & Rosendahl, B. R. (1989). Relationships between pre-rift structure and rift  
 830 architecture in Lakes Tanganyika and Malawi, East Africa. *Nature*.  
 831 <https://doi.org/10.1038/337354a0>
- 832 Wallace, R. E. (1951). Geometry of shearing stress and relation to faulting. *The Journal of*  
 833 *Geology*, 59(2), 118–130.

- 834 Walshaw, R. D. (1965). The Geology of the Nchue-Balaka Area. *Bulletin of the Geological*  
835 *Survey, Malawi, 19.*
- 836 Wedmore, L., Biggs, J., Williams, J. N., Fagereng, Å., Dulanya, Z., Mphepo, F., & Mdala, H.  
837 (8888). Distributed active fault scarps in southern Malawi and the implications for the  
838 evolution of strain in amagmatic continental rifts.
- 839 Wheeler, W. H., & Rosendahl, B. R. (1994). Geometry of the Livingstone Mountains Border  
840 Fault, Nyasa (Malawi) Rift, East Africa. *Tectonics, 13*(2), 303–312.  
841 <https://doi.org/10.1029/93TC02314>
- 842 Williams, J. N., Toy, V. G., Massiot, C., McNamara, D. D., Smith, S. A. F., & Mills, S.  
843 (2018). Controls on fault zone structure and brittle fracturing in the foliated hanging  
844 wall of the Alpine Fault. *Solid Earth, 9*(2), 469–489. [https://doi.org/10.5194/se-9-469-](https://doi.org/10.5194/se-9-469-2018)  
845 [2018](https://doi.org/10.5194/se-9-469-2018)
- 846 Withjack, M. O., & Jamison, W. R. (1986). Deformation produced by oblique rifting.  
847 *Tectonophysics*. [https://doi.org/10.1016/0040-1951\(86\)90222-2](https://doi.org/10.1016/0040-1951(86)90222-2)  
848  
849

850 **List of figures**

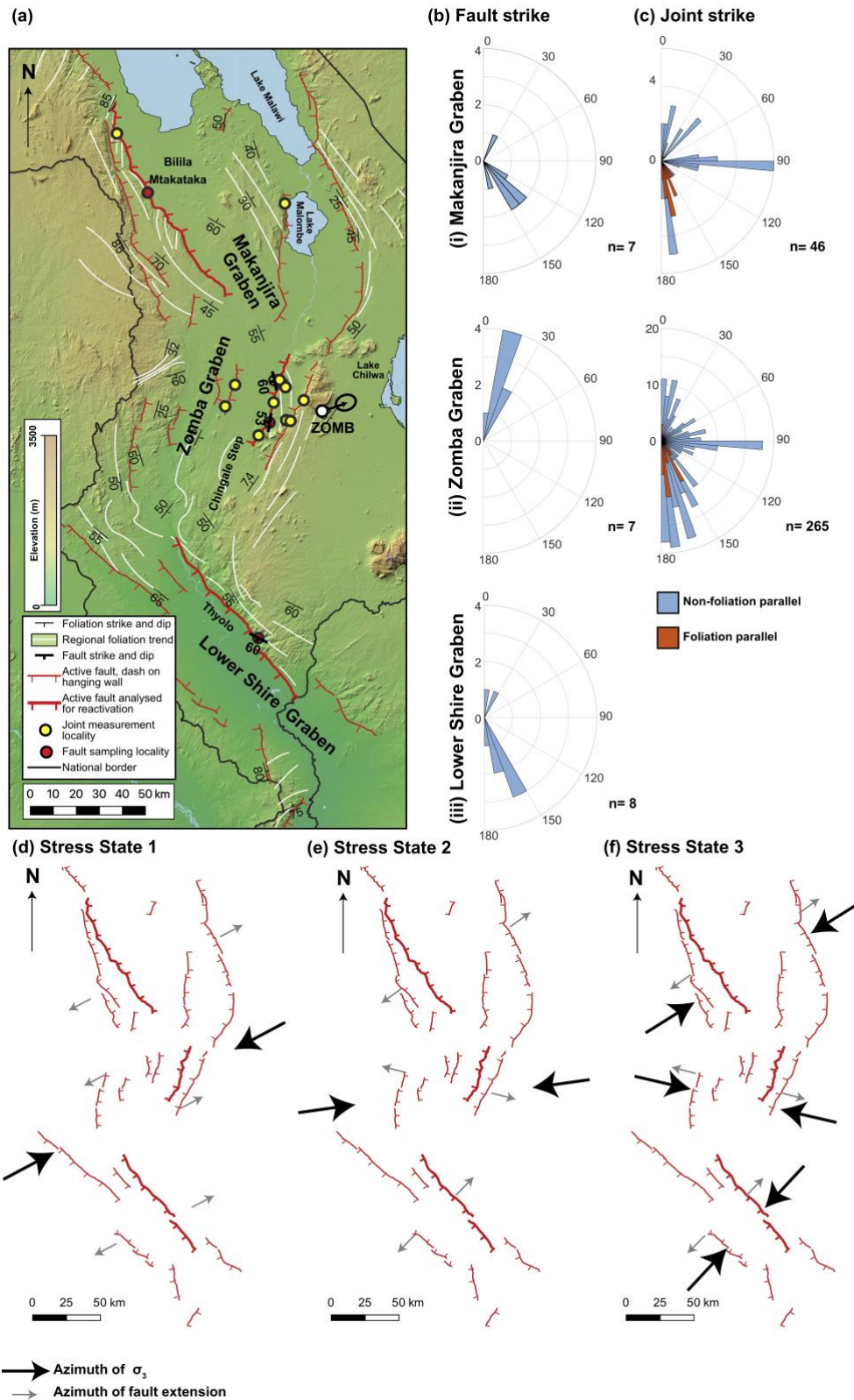
851 Figure 1



852

853 Figure 1: (a) Location of Malawi Rift within East Africa. (b) Simplified geological map of  
 854 the rift with Proterozoic units taken from *Fritz et al.*, [2013], and underlain by Shuttle Radar  
 855 Topography Mission (SRTM) 30 m digital elevation model (DEM; *Sandwell et al.*, [2011]).  
 856 Location of focal mechanisms listed in Table 1 also given. Foliation orientations and trends  
 857 collated from SRTM images, field measurements and previous studies [*Bloomfield*, 1958,  
 858 1965; *Bloomfield & Garson*, 1965; *Habgood et al.*, 1973; *Hodge et al.*, 2018].

859 Figure 2



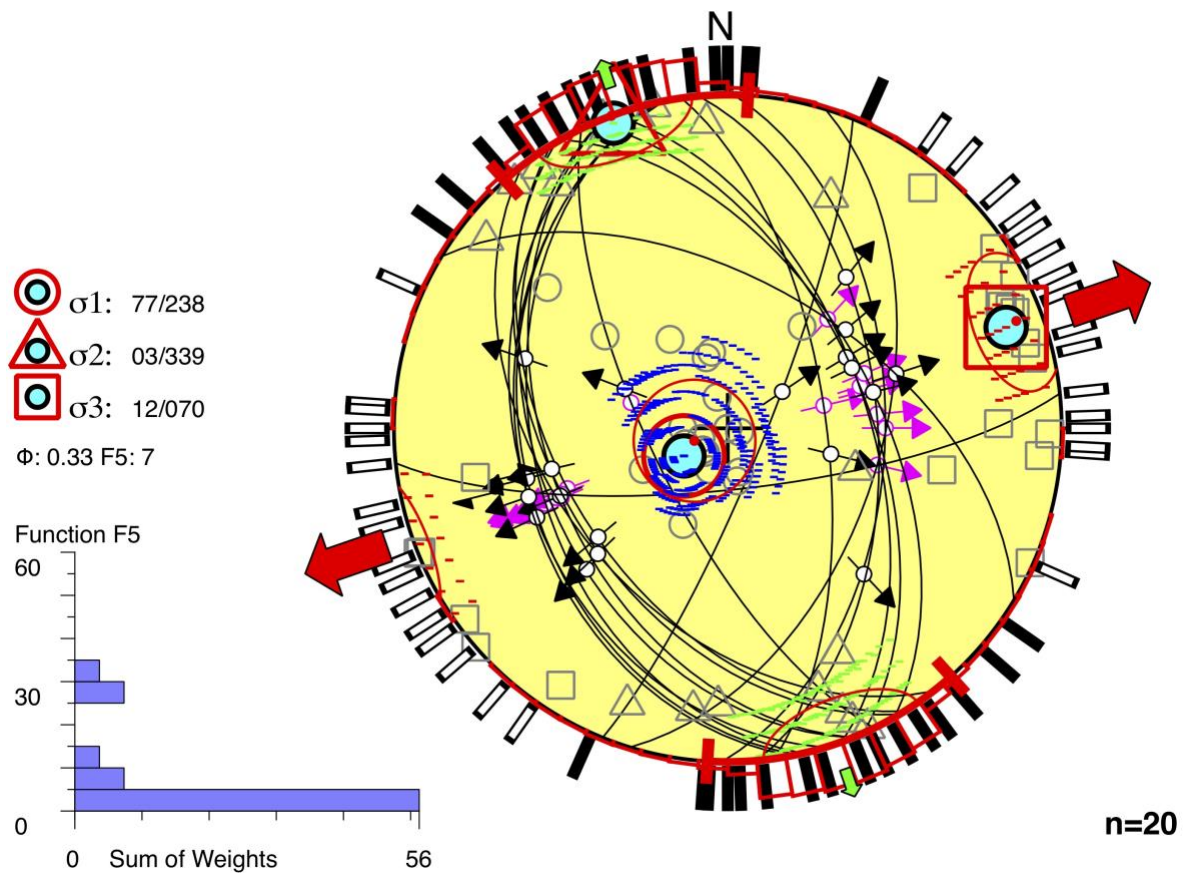
860

861 Figure 2: (a) Map of active faults in southern Malawi collated from TanDEM-X DEM and geological  
 862 maps [Bloomfield, 1958, 1965; Bloomfield and Garson, 1965; Walshaw, 1965; Habgood et al., 1973;  
 863 Hodge et al., 2018, 2019; Wedmore et al., in prep.]. Area shown is indicated in Figure 1b. The  
 864 azimuth of the ZOMB permanent GPS station is also shown [Stamps et al., 2018]. Joint and fault

865 sampling and measurement localities also shown. Rose plots for measurements of (b) fault and (c)  
866 joint strike for each of the grabens. Schematic representation of the  $\sigma_3$  azimuth in Stress States (d) 1,  
867 (e) 2, and (f) 3 with respect to faults in southern Malawi. In addition, we show extension direction as  
868 inferred by the Wallace Bott criterion (for Stress States 1 and 3), or if a slip reorientation occurs (for  
869 Stress State 2; *Philippon et al.*, [2015]). Area shown for each map is the same as in (a). Weighted  
870 fault lines are those on which reactivation analysis was conducted.

871

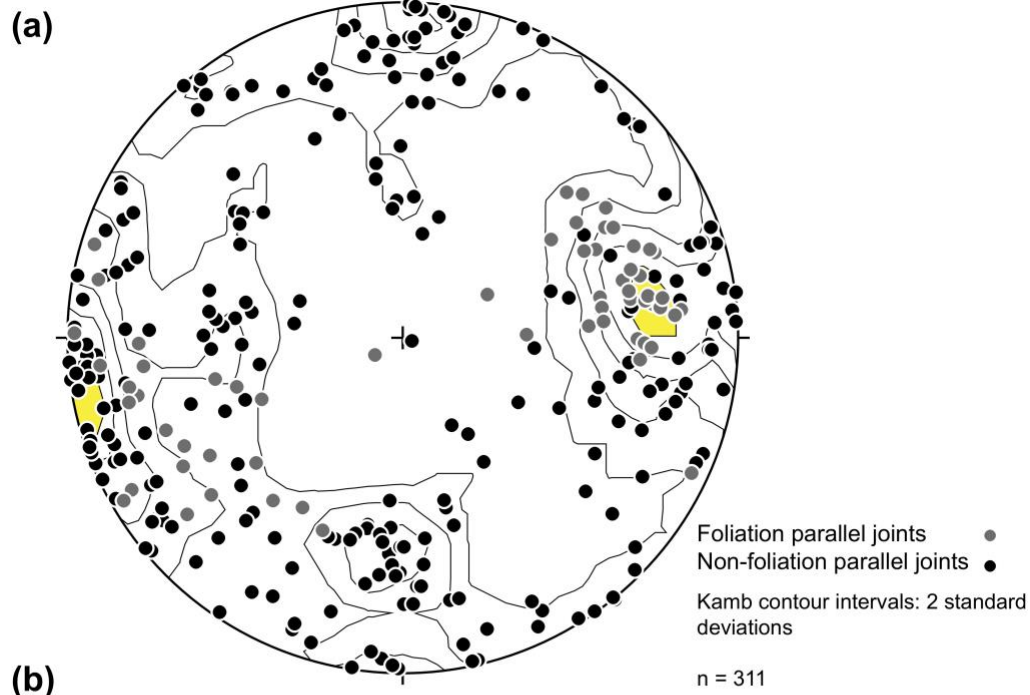
872 Figure 3



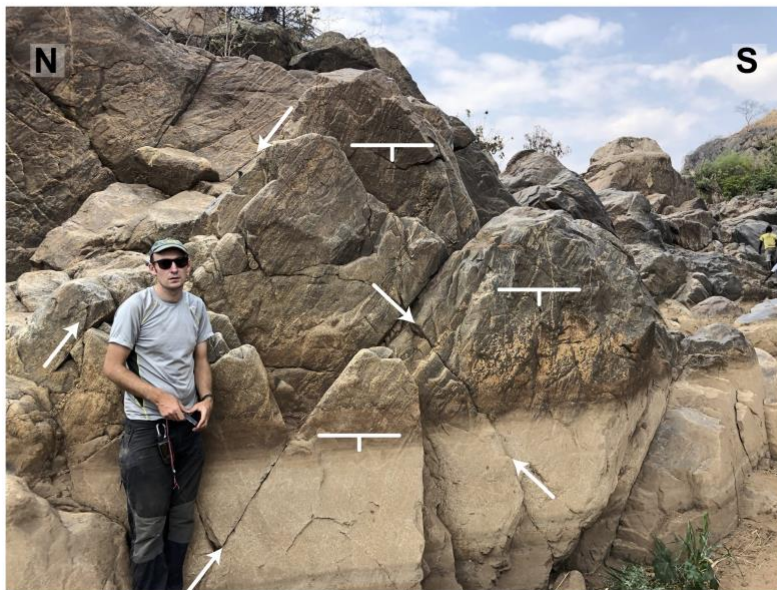
873  
 874 Figure 3: Results of earthquake focal mechanism stress inversion for the Malawi Rift using  
 875 Win-Tensor [Delvaux & Sperner, 2003] and the mechanisms listed in Table 1. Lower-  
 876 hemisphere equal area stereoplot depicts selected nodal planes (black lines) with slip vectors  
 877 (black arrows), the three principal stress axes (blue circles), maximum and minimum  
 878 horizontal stress ( $S_{Hmax}$  and  $S_{Hmin}$ ) trajectories (small green and large red arrows),  $S_{Hmax}$  and  
 879  $S_{Hmin}$  trajectories for individual focal mechanisms (black and white bars outside stereoplot),  
 880 and kinematic axes for individual focal mechanisms (grey circle:  $p$  axis, triangle:  $b$  axis,  
 881 square:  $t$  axis). Histogram represents distribution of misfit angles ( $\omega$ ), weighted arithmetically  
 882 according to magnitude.

883

884 Figure 4



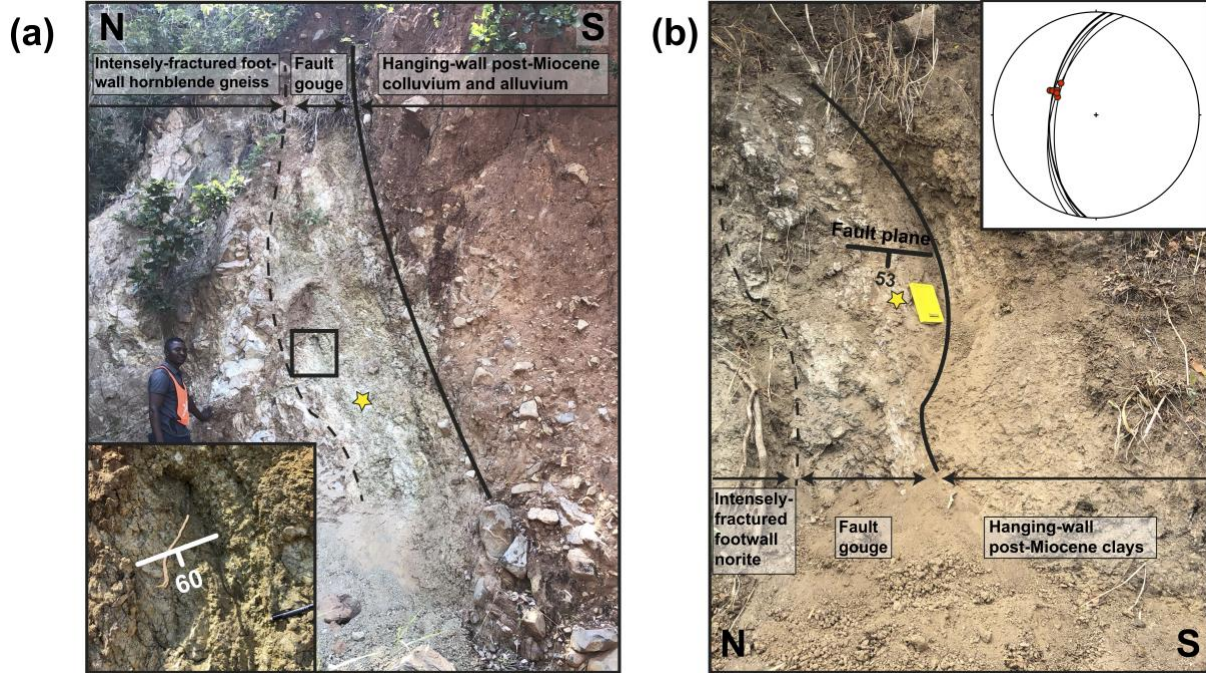
(b)



885  
 886  
 887  
 888  
 889  
 890  
 891

Figure 4: (a) Stereoplot showing poles to joint orientations that were also shown in Figure 2c. Shaded contour interval indicates highest concentration of the N-S striking joints. The trend at the centre of this interval ( $082^\circ$ ) is used to infer the trend of the minimum principal stress ( $\sigma_3$ ) for Stress State 2. The range of this interval  $\pm 7^\circ$ . (b) Examples of joint sets in the Malawi Rift. The joint set the facing the photo is a steeply dipping N-S set, which are mutually cross cutting with an inclined E-W set.

892 Figure 5

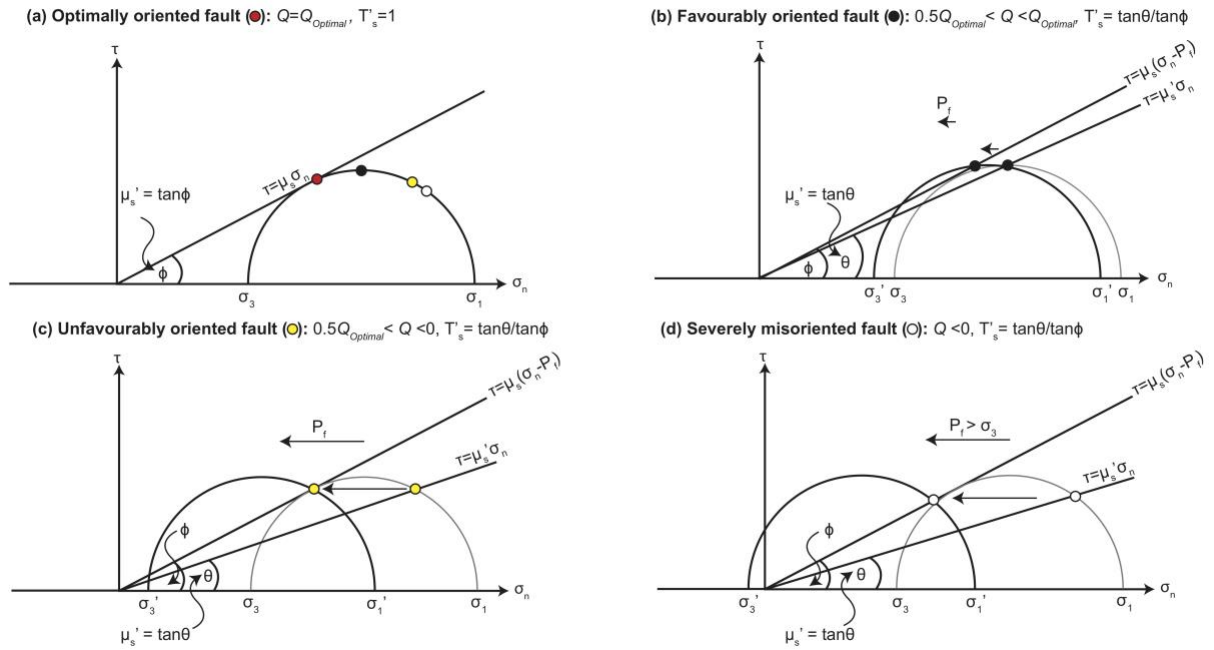


893

894 Figure 5: Examples of outcrops from (a) the Thyolo and (b) Chingale Step faults. Stars depict  
 895 where ‘fault rock’ samples were taken from for these faults. Footwall and hanging-wall unit  
 896 descriptions taken from *Habgood et al.*, [1973] and *Bloomfield*, [1965] respectively. Box in  
 897 (a) highlights plane that was used to measure dip of Thyolo fault and is shown in the inset.  
 898 Inset in (b) shows fault slickenside orientations [*Wedmore et al.*, in prep.]. Note, a dip of  $57^\circ$   
 899 was used for the Chingale Step fault reactivation analysis, based on the average dip measured  
 900 over other sites (Figure 2a).

901

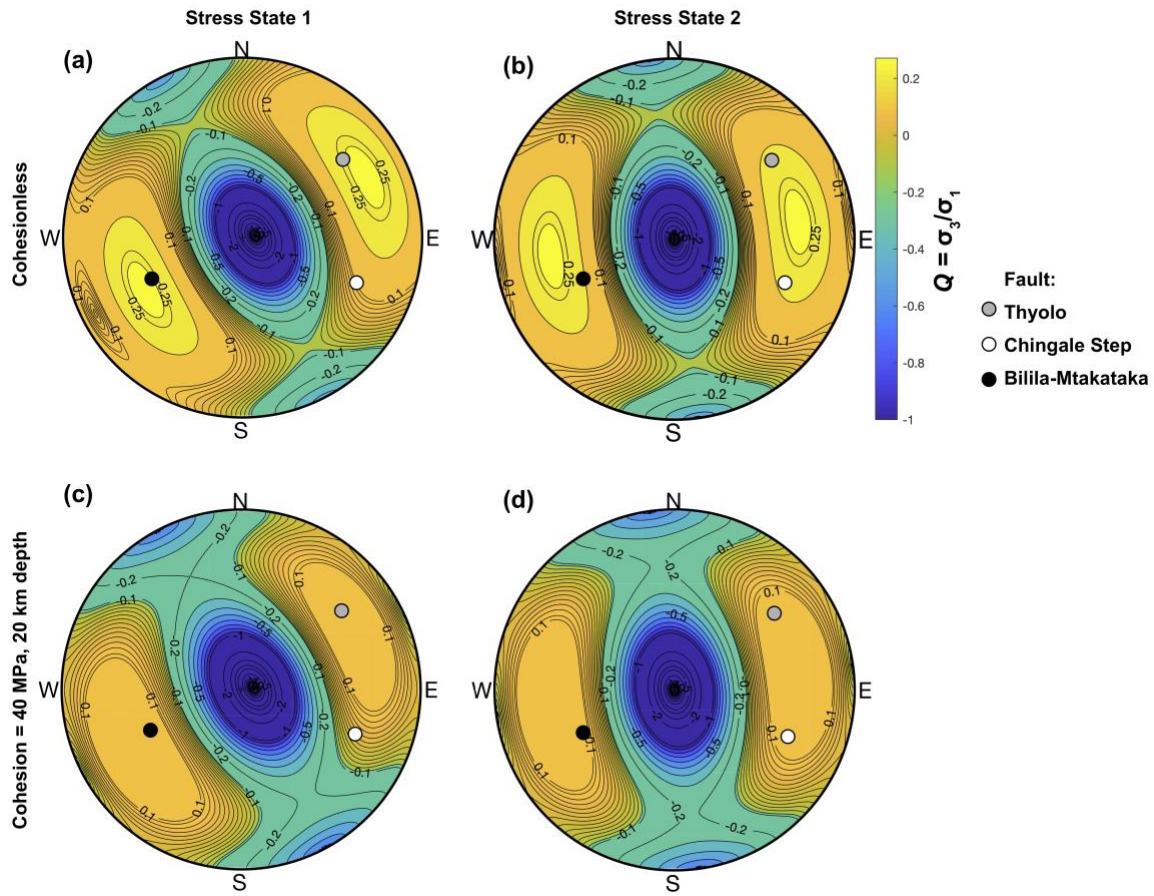
902 Figure 6



903  
 904  
 905  
 906  
 907  
 908  
 909  
 910  
 911  
 912  
 913

Figure 6: Illustration in Mohr Space of different concepts for analysing fault reactivation. (a) The stress ratio ( $Q = \sigma_3/\sigma_1$ ), normalized slip tendency ( $T'_s$ ), and effective coefficient of friction ( $\mu_s'$ ) acting on an optimally-oriented cohesionless fault. In this case,  $Q = Q_{Optimal}$ ,  $T'_s = 1$ ,  $\mu_s'$  is the same as the frictional strength of an optimally oriented fault ( $\mu_s = \tan\phi$ ), and no fluid pressure ( $P_f$ ) is required for reactivation. In addition, the orientation of three hypothetical faults is also depicted. The  $Q$ ,  $T'_s$ ,  $\mu_s'$ , and  $P_f$  required for reactivation of these (b) favourably oriented, (c) unfavourably oriented, and (d) severely misoriented fault is then also shown. For clarity, this example is for a 2D reactivation analysis when the fault plane contains  $\sigma_2$ . However, the principles are the same for a 3D analysis.

914 Figure 7

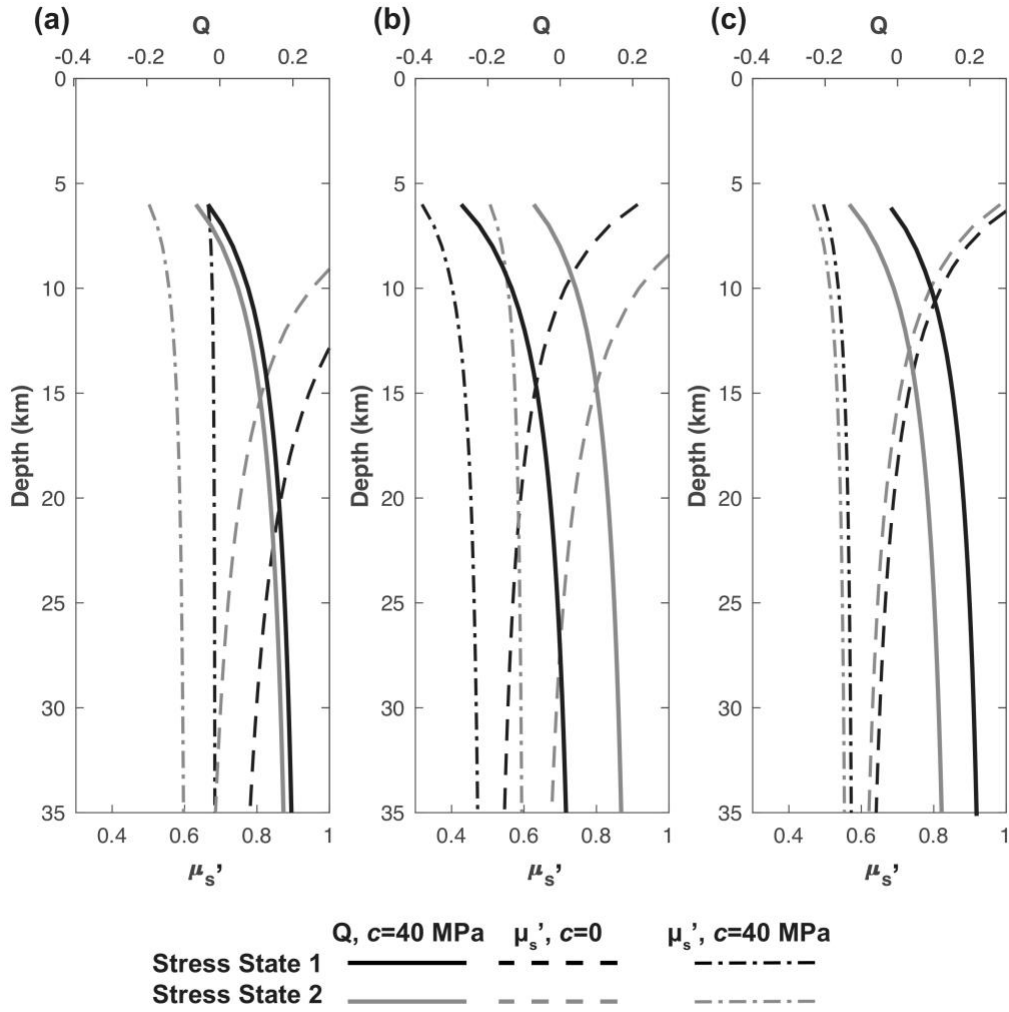


915

916 Figure 7: Stereoplots contoured by stress ratio ( $Q=\sigma_3/\sigma_1$ ) required for fault reactivation in  
 917 Stress States 1 and 2 [Leclère & Fabbri, 2013]. Both (a&b) cohesionless and (c&d) cohesive  
 918 are considered. Results pertain to any depth for cohesionless faults and are calculated for a  
 919 depth of 20 km for cohesive faults, assuming the density model for the rift outlined in Table  
 920 S2. For all plots  $\mu_s=0.7$  and  $\Phi=0.33$ . Poles to the fault orientations analyzed here are also  
 921 shown.

922

923 Figure 8



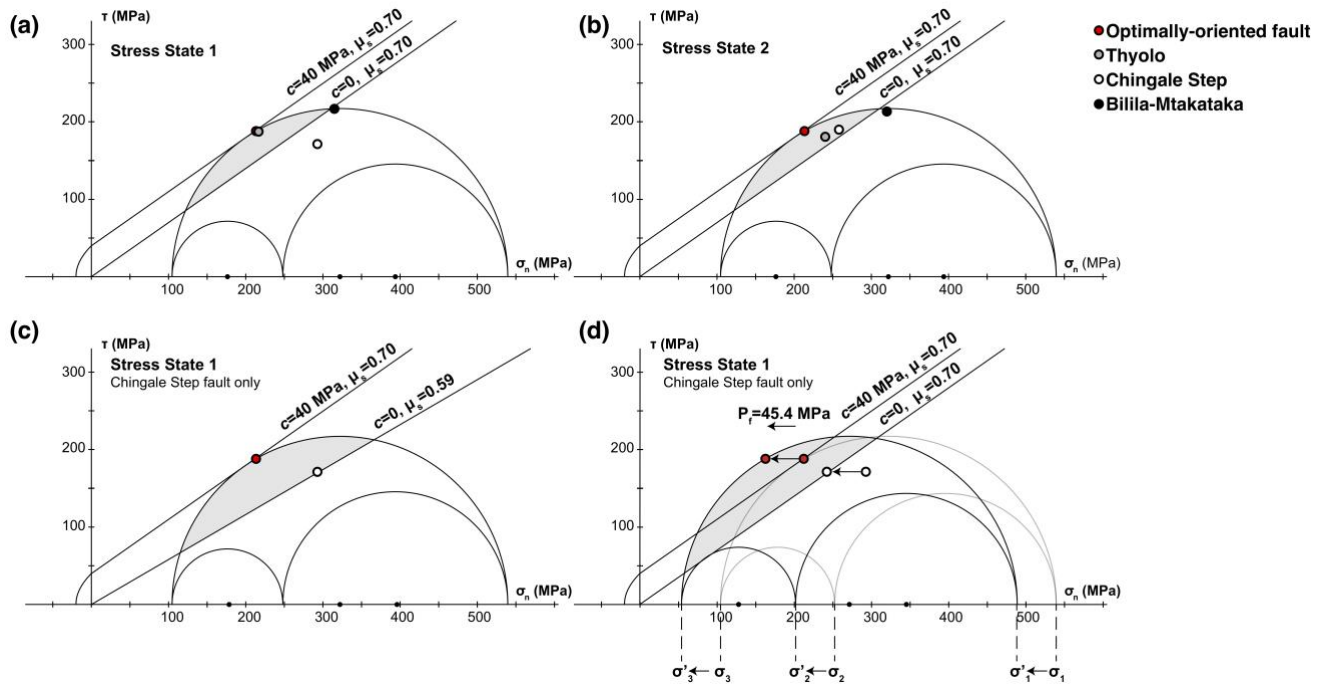
924

925 Figure 8: The stress ratio ( $Q=\sigma_3/\sigma_1$ ) and effective coefficient of friction ( $\mu_s'$ ) of (a) Thyolo,  
 926 (b) Chingale Step, and (c) Bilila-Mtakataka fault for Stress States 1 and 2 between depths 6-  
 927 35 km. For cohesionless faults,  $Q$  does not vary as a function of depth and so is not shown.

928 Only values where  $\mu_s' < 1$  are plotted.

929

930 Figure 9

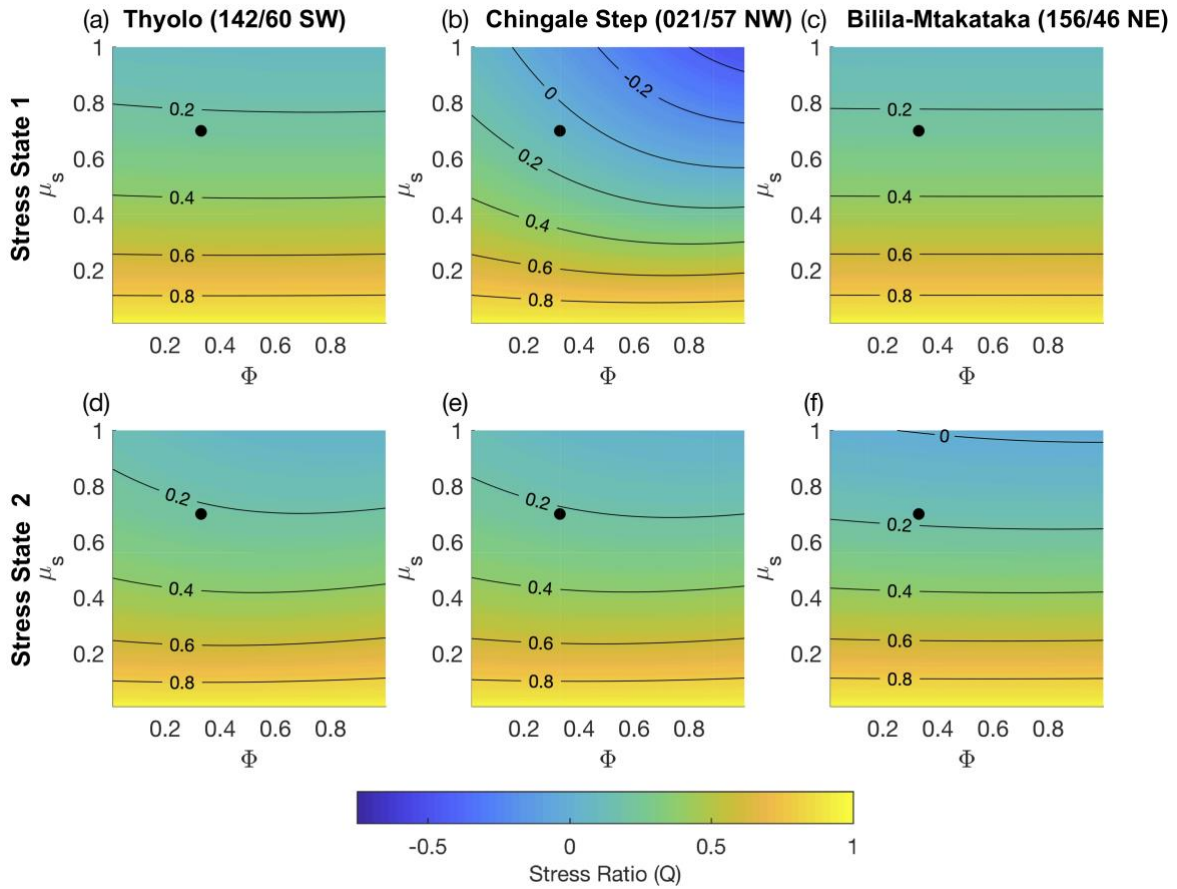


931

932 Figure 9: 3D Mohr Circle analysis for reactivation of faults in southern Malawi at 20 km  
 933 depth. Shaded region in each plot depicts range of orientations where a cohesionless fault will  
 934 reactivate. (a) Orientation of Thyolo, Chingale Step and Bilila-Mtakataka Fault in Stress  
 935 States 1. Given the failure criteria assumed here, only the Thyolo and Bilila-Mtakataka  
 936 fault will reactivate. (b) Same as (a) but for Stress State 2. The Thyolo and Chingale Step  
 937 faults will reactivate in this stress state and reactivation of Bilila-Mtakataka requires a slight  
 938 reduction in  $\mu_s'$  to 0.67 (Table 3). Reactivation of cohesionless Chingale Step fault in Stress  
 939 State 1 at 20 km depth requires that (c)  $\mu_s'=0.59$  or that (d)  $P_f'=45.4$  MPa (equivalent to  
 940  $\lambda_v'=0.08$ ).

941

942 Figure 10



943

944 Figure 10: Contour plots for stress ratio ( $Q=\sigma_3/\sigma_1$ ) needed for reactivation of a cohesionless  
 945 fault in frictional strength-stress shape ratio ( $\mu_s$ - $\Phi$ ) space for the given fault orientations and  
 946 Stress States 1 and 2. Black circle represents point where  $\Phi=0.33$  and  $\mu_s=0.70$ , as is used in  
 947 Figure 7. For similar analysis for cohesive fault, see Figure S8.

948

949

950 **List of tables**951 **Table 1**

<b>Date</b> <b>(yyyy/mm/dd)</b>	<b>M<sub>w</sub></b>	<b>Longitude</b>	<b>Latitude</b>	<b>Depth</b> <b>(km)</b>	<b>Catalogue</b>	<b>Strike</b>	<b>Dip</b>	<b>Rake</b>	<b>Rejected</b>	<b>Misfit</b> <b>(°)</b>	<b>Notes</b>
1954/01/17	6.7	36.00	-16.5.0	20	DB2010	197	68	164	Y		
1966/05/06	5.1	34.60	-15.70	17	DB2010	001	51	-56		31	
1978/01/08	4.9	34.45	-11.76	15	DB2010	338	45	-90		0	
1989/03/09	5.5	34.47	-13.68	31	C2011	340	56	-99		2.6	Same as event 4 in DB2010
1989/03/10	6.1	34.49	-13.71	32	C2011	336	56	-92		1.2	Same as event 5 in DB2010
1989/09/05	5.4	34.46	-11.8	19.8	DB2010	063	52	149	Y		
1994/11/16	4.5	33.51	-9.42	7	C2011	301	64	-11	Y		Focal mechanism from gCMT
1995/07/22	4.9	34.84	-13.98	33	C2011	158	42	-105		7.3	
1995/09/30	4.7	34.40	-13.82	30	C2011	140	38	-75		2.4	
1996/08/30	4.5	34.10	-15.40	10	DB2010	071	27	-46		0.5	
1998/08/24	4.7	34.89	-13.77	44	C2011	163	37	-95		0.3	Same as event 7 in DB2010
1999/09/01	4.7	34.2	-10.10	10	DB2010	022	81	-144		3.7	
2000/01/04	4.8	36.10	-16.10	25	DB2010	352	66	-70		3.7	
2002/08/31	5.0	9.84	34.23	20	C2011	355	53	-126		28	Same as event 9 in DB2010
2004/03/14	4.8	34.35	-10.08	29	DB2010	017	52	-117		13.6	
2004/08/21	4.7	34.44	-10.60	12	DB2010	084	75	-17		4.1	
2009/12/06	5.7	-10.13	33.85	6	C2011	168	38	-91		1.2	
2009/12/09	5.8	-9.95	33.88	6	C2011	167	41	-70		27	
2009/12/11	4.9	-10.09	33.86	8	C2011	148	48	-96		4.4	Focal mechanism from gCMT

2009/12/12	5.5	-9.94	33.91	4	C2011	169	37	-95	0.4
2009/12/19	5.9	-10.11	33.82	5	C2011	149	46	-77	1
2018/03/08	5.5	35.427	-16.76	17	USGS	142	45	-94	6.4
2018/03/08	4.9	35.486	-16.83	10	USGS	330	54	-77	1.6

952 Table 1: Compilation of earthquake focal mechanisms for the Malawi Rift. Catalogue codes are: (1) DB2010, *Delvaux and Barth*, [2010] and  
953 references therein, (2) C2011, *Craig et al.*, (2011) and references therein, (3) USGS, *U.S. Department of the Interior U.S. Geological Survey*,  
954 [2018]. Focal mechanisms from C2011 are from waveform modelling unless otherwise stated. The reported nodal plane is the one favoured by  
955 the stress inversion (i.e. the plane with the smallest misfit, the magnitude of which is also reported). We also indicate which mechanisms were  
956 filtered during the stress inversion. Map of focal mechanisms is given in Figure 1.

957

958 Table 2

<b>Fault</b>	<b>Sample</b>	<b>Quartz</b>	<b>Albite</b>	<b>Biotite</b>	<b>Muscovite</b>	<b>Actinolite</b>	<b>Kaolinite</b>	<b>Montmorillonite</b>	<b>Dolomite</b>	<b>Prehnite</b>	<b>Calcite</b>
Thyolo	Country rock	43	40			14	3				
	Fault rock	81					8	5		6	
Chingale Step	Country rock	30	30	37			3				
	Fault rock	4						2	1		93
Bilila-Mtakataka	Country rock	11	52		8	26	3				
	Fault rock	74	16								10

959 Table 2: Quantitative XRD (as weight %) of samples collected from fault zones in the Malawi Rift. Results are normalized to 100% and so do  
 960 not include estimates of unidentified or amorphous material. XRD diffractograms are given in Figure S5.

961

962

Fault	Fault orientation	Stress State	Stress Ratio ( $Q$ )		Slip tendency ( $T_s$ )	Normalized slip tendency ( $T'_s$ )	Effective coefficient of friction ( $\mu_s'$ )	
			$c=0$	$c=40$ MPa			$c=0$	$c=40$ MPa
Thyolo	142/60 SW	1	0.24	0.16	0.65	0.92	0.87	0.68
		2	0.22	0.14	0.61	0.87	0.75	0.59
Chingale Step	021/57 NW	1	0.07	-0.02	0.47	0.67	0.59	0.45
		2	0.21	0.13	0.60	0.86	0.74	0.58
Bilila-Mtakataka	156/46 NE	1	0.17	0.16	0.65	0.93	0.69	0.56
		2	0.24	0.08	0.57	0.81	0.67	0.54

963 Table 3: Results of fault reactivation analysis in terms of the stress ratio ( $Q$ ) of each fault with respect to Stress States 1 and 2, slip tendency ( $T_s$ ),  
964 normalized slip tendency ( $T'_s$ ), and effective frictional strength ( $\mu_s'$ ) needed to reactivate them.  $T_s$ ,  $T'_s$ , and  $Q$  where  $c=0$  pertain to any depth.  $Q$   
965 where  $c=40$  MPa and  $\mu_s'$  are for a depth of 20 km, and assume a fault surrounded by intact rock where  $\mu_{s\text{-intact}}=0.7$ . See Figure 8 for how these  
966 values vary with depth. All results to 2 decimal places.

967

968